Global and Planetary Change 197 (2021) 103389

Contents lists available at ScienceDirect

Global and Planetary Change

journal homepage: www.elsevier.com/locate/gloplacha

Effect of metasomatism on the electrical resistivity of the lithospheric mantle – An integrated research using magnetotelluric sounding and xenoliths beneath the Nógrád-Gömör Volcanic Field

Levente Patkó [a,b,c,d], Attila Novák [b,d], Rita Klébesz [d], Nóra Liptai [b], Thomas Pieter Lange [a,b], Gábor Molnár [d,e], László Csontos [f], Viktor Wesztergom [b,d], István János Kovács [b,d], Csaba Szabó [a,d,*]

[a] Lithosphere Fluid Research Lab (LRG), Eötvös Loránd University, Budapest, Hungary
[b] Lendület Pannon LitH$_2$Oscope Research Group, Research Centre for Astronomy and Earth Sciences (CSFK), Sopron, Hungary
[c] Isotope Climatology and Environmental Research Centre, Institute for Nuclear Research (ATOMKI), Debrecen, Hungary
[d] Geodetic and Geophysical Institute, Research Centre for Astronomy and Earth Sciences (CSFK), Sopron, Hungary
[e] Geological, Geophysical and Space Research Group of the Hungarian Academy of Sciences, Eötvös Loránd University, Budapest, Hungary
[f] Exploration & Production Division, MOL Group, Budapest, Hungary

ARTICLE INFO

Keywords:
Long period magnetotellurics
Upper mantle xenoliths
Low electrical resistivity
Mantle metasomatism
Wehrlitization

ABSTRACT

Long period magnetotelluric (MT) data were collected at 14 locations along a ~50 km long NNW-SSE profile in the Nógrád-Gömör Volcanic Field (NGVF), which is one of the five mantle xenolith bearing Neogene alkali basalt locations in the Carpathian-Pannonian region. As a result, a low resistivity anomaly (<10 Ωm) was observed approximately at 30–60 km depth beneath the central part of the NGVF, indicating the presence of a conductive body beneath the Moho. This is the same area where upper mantle xenoliths with wehrlitic modal composition were collected from six quarries. The wehrlites were formed as a result of mantle metasomatism involving the peridotite wall rock and a mafic melt. The spatial coincidence of the geophysical anomaly and the petrographic-geochemical alteration in the upper mantle suggests their probable relationship. To test this assumption, we estimated the electrical resistivity of the wehrlites. The outcome reveals lower electrical resistivity for wehrlites (~132 Ωm) compared to the non-metasomatized lherzolites (~273 Ωm) from the same localities. However, it is still higher than the values acquired with long period MT soundings. Thus, further modelling was implemented in order to test the possible role of melt. The models revealed that even ~2–3 vol.% of interconnected melt is enough to lower the electrical resistivity below 1 Ωm in the wehrlites. The interconnected glass phase found in the wehrlites may be the evidence for this later solidified melt. All these suggest that melts may still be present in small amounts beneath the cooling NGVF. The intensive melt upwelling in the central part of the NGVF resulting in a wehrlitized mantle portion with low electrical resistivity, as well as the extensive basalt flows on the surface, can be explained by deep deformation zones, which provide excellent migration pathways for melts through the entire lithosphere.

1. Introduction

Magnetotellurics (MT) is routinely used both in the industrial and academic research. In mineral, hydrocarbon and geothermal explorations, audio-MT studies are applied mostly for shallow crustal (i.e. 250–2000 m) depths (e.g. Strangway et al., 1973; Aiken and Ander, 1981; Orange, 1989). In academic studies, MT is usually used for addressing a specific geological problem and the investigated depth usually ranges from a few tens of kilometers up to ~200 km. These studies aim to define compositions, structures and processes in the crust and in the upper mantle (Hautot et al., 2000; Selway et al., 2009; Muller et al., 2009; Bologna et al., 2011; Ádám et al., 2017; Evans et al., 2019). MT is especially sensitive to detect partial melts/fluids by quantifying resistivity (Wannamaker et al., 2002; Hill et al., 2009; Becken and Ritter, 2012; Selway et al., 2019), and it is commonly applied to detect the lithosphere–asthenosphere boundary (LAB) or other surfaces in the

* Corresponding author.
E-mail address: cszabo@elte.hu (C. Szabó).

https://doi.org/10.1016/j.gloplacha.2020.103389
Received 15 May 2020; Received in revised form 20 November 2020; Accepted 21 November 2020
Available online 4 December 2020

mantle characterized by changes in electrical resistivity due to physico-chemical changes (e.g. Praus et al., 1990; Eaton et al., 2009; Jones et al., 2010). Even though the resolution of MT deep sounding becomes gradually worse with increasing depth and measurements can be challenging due to the presence of shallow, slightly resistive layers, good resolution can be achieved even at great depths (>30 km) with careful planning of station density and adequate data processing. Furthermore, several case studies show that far more information can be extracted by combining electrical models with petrologic data than only considering the resistivity distribution within the studied volume (Khan et al., 2006; Fullea et al., 2011; Jones et al., 2012; Vozár et al., 2014).

In this paper, we investigated whether the assumed lithological heterogeneities and/or the presence of melt/fluid in the lithospheric mantle beneath the Nógrád-Gömör Volcanic Field (NGVF) (Fig. 1) can be studied by MT. The NGVF is the northernmost of the five, mantle xenolith-bearing alkali basalt volcanic fields in the Carpathian-Pannonian region (CPR) (Fig. 1a). The spatial distribution of the xenoliths and their petrographic and geochemical characteristics are well known (Szabó and Taylor, 1994; Liptai et al., 2017; Patkó et al., 2020a). The dominant lithology in the mantle is lherzolite (~75% of all xenoliths), however, the large number of wehrlite xenoliths (~20% of all xenoliths) and the detailed geochemical study of the lherzolite xenoliths indicate that the upper mantle beneath the NGVF was affected by several metasomatic events, the last of which caused the formation of the wehrlites (Liptai et al., 2017; Patkó et al., 2020a). However, xenoliths are only fragments of the lithospheric mantle and the spatial distribution of this metasomatized mantle domain is unknown. Thus, the goal of this study was to image the lithospheric mantle of the NGVF, map the LAB, and determine whether the distribution of the lithological differences can be constrained by MT. We provide a geological interpretation for the MT data obtained along a profile across the study area (Fig. 1b), using theoretical calculations to compare the electrical resistivity with compositional differences of the peridotite. In the electrical resistivity modelling, the presence of melt/fluid is also taken into account. This case study of combined geological and geophysical methods may help interpreting deep MT results worldwide, even where mantle xenolith data are not available. Our research delivers information on the root zone of an intraplate volcanic field, where the magmatism may be more extensive and longer lasting even after the latest active eruptions than it was previously thought based only on the areal extent and volume of erupted products.

2. Geological settings

The Pannonian Basin is situated in East-Central Europe surrounded by the Alpine, Carpathian and Dinaric orogenic chains (Fig. 1a). It consists of two tectonic megaunits, ALCAPA in the northwest with Mediterranean affinity and Tisza-Dacia in the southeast with dominantly European origin, which are divided by the Middle Hungarian Shear zone (Stegena et al., 1975; Balla, 1984; Kázmér and Kovács, 1985; Fodor et al., 1999; Csontos and Vörös, 2004). The NGVF is located at the northern edge of the Pannonian Basin (Fig. 1a) on the ALCAPA megaunit. The Gemeric and Veporic sub-units (in fact Alpine nappes within ALCAPA) comprise the basement of the NGVF, consisting mostly of Paleozoic and Mesozoic sequences, and sheared and tectonized crystalline nappes (Tomek, 1993; Koroknai et al., 2001). In the cover sequence, there are Tertiary sediments and volcanic rocks such as Miocene andesites and Plio-Pleistocene alkali basalts and their pyroclasts (Fig. 1b). The alkali basalt products of the NGVF consist of maars, diatremes, tuff cones, cinder/spatter cones and lava flows, which are dispersed in an area of ~150 km^2 (Konečný et al., 1995a). The formation of alkali basalts is related to post-extensional thermal relaxation of the asthenosphere, which is the source of these melts as a result of small degree partial melting (<5%) (Embey-Isztin et al., 1993; Harangi, 2001; Lexa et al., 2010). It has been recently proposed that compression in the tectonic inversion stage of the CPR evolution may have squeezed partial

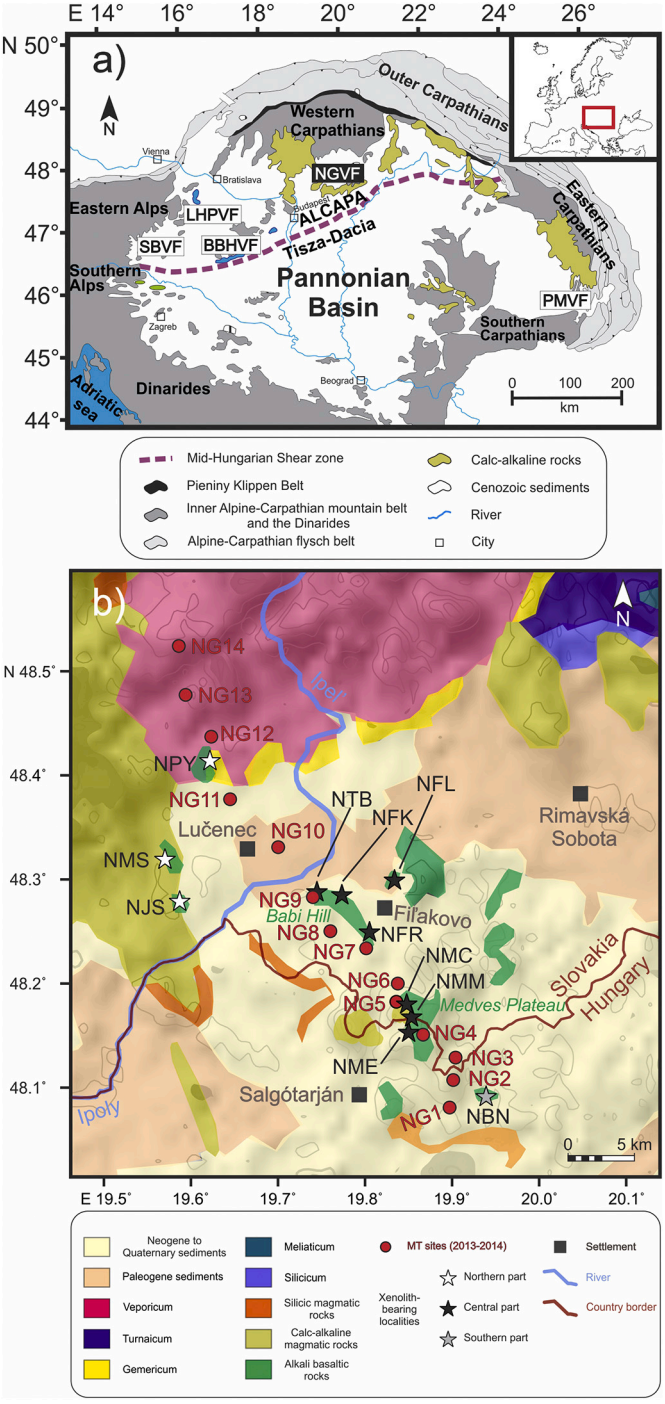

Fig. 1. (a) Simplified geological map of the Carpathian-Pannonian region (CPR) with the inferred ALCAPA–Tisza-Dacia microplate boundary (after Csontos and Nagymarosy, 1998 and references therein). Xenolith-bearing Neogene alkali basalt volcanic fields shown are the following: SBVF - Styrian Basin Volcanic Field; LHPVF - Little Hungarian Plain Volcanic Field; BBHVF - Bakony–Balaton Highland Volcanic Field; NGVF - Nógrád-Gömör Volcanic Field; PMVF - Perşani Mountains Volcanic Field. (b) Simplified geological map of the Nógrád-Gömör Volcanic Field (modified after Hók et al. (2014) and Lexa et al. (2000)) with the position of xenolith sampling localities (black star) and magnetotelluric stations (red circle). Xenolith sampling quarries from NW to SE are the following: Podrečany (NPY), Mašková (NMS), Jelšovec (NJS), Trebeľovce (NTB), Fiľakovské Kováče (NFK), Fiľakovo-Kerčik (NFL), Ratka (NFR), Mačacia (NMC), Magyarbánya (NMM), Eresztvény (NME) and Bárna-Nagykő (NBN). (For interpretation of the references to color in this figure legend, the reader is referred to the web version of this article.)

melt out from the asthenosphere (Kovács et al., 2020).

The volcanic activity in the NGVF took place between 6.17–1.35 Ma based on K-Ar dating (Balogh et al., 1981). New results of combined U/Pb and (U–Th)/He geochronometry (Hurai et al., 2013) have slightly extended the period of volcanism (7–0.3 Ma). Mantle xenoliths are abundant in the alkali basalt at NGVF from Podrečany (NPY) in the northwest to Bárna (NBN) in the southeast (Fig. 1b), however they are absent in the mafic volcanics east of Fil'akovo. These mantle xenoliths have variable compositions, with samples belonging to the Cr-diopside (Hovorka and Fejdi, 1980; Szabó and Taylor, 1994; Konečný et al., 1995b; Liptai et al., 2017; Patkó et al., 2020a) and Al-augite (Kovács et al., 2004; Zajacz et al., 2007) series defined by Wilshire and Shervais (1975). Among the Cr-diopside rocks, a lherzolitic and wehrlitic series were distinguished (Liptai et al., 2017; Patkó et al., 2020a), the latter only present in the central outcrops NGVF (Babi Hill and Medves Plateau; Fig. 1b).

3. Method

Magnetotellurics (MT) is based on the ultra and extremely low frequency (ULF-ELF) geomagnetic field time variation and its response to the conductive Earth according to the Faraday law of induction

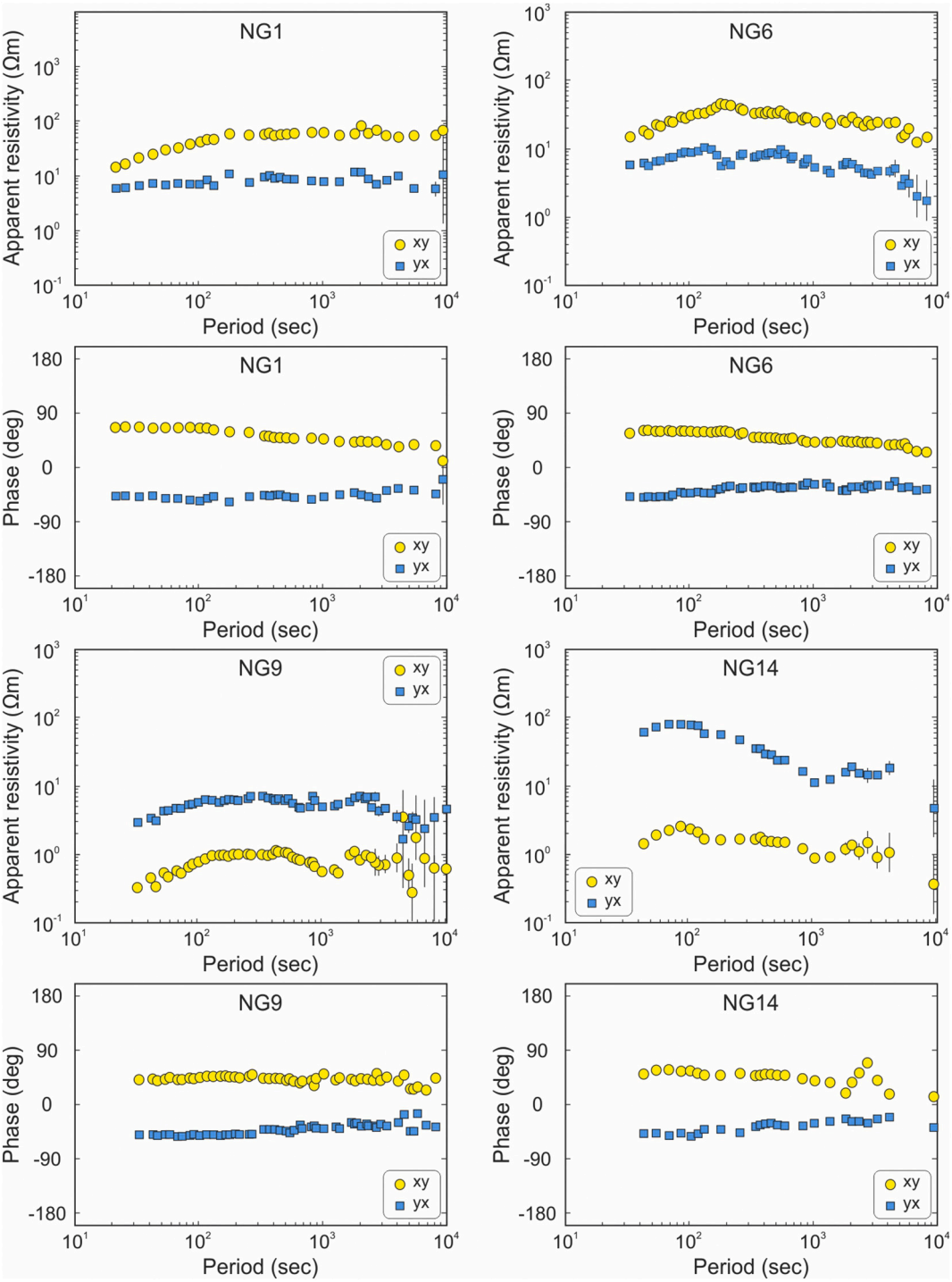

Fig. 2. Characteristic raw magnetotelluric sounding curves of apparent resistivities and impedance phases at four selected sites: NG1, NG6, NG9, NG14.

(Tikhonov, 1950; Cagniard, 1953). The penetration depth of the electromagnetic (EM) waves depends on the period and resistivity of materials. The EM field observed on the surface is the superposition of primary (ionospheric, magnetospheric current system) and secondary (subsurface induction) sources. The induction effect (i.e. EM properties of the subsurface) is detectable on the surface in the form of impedance tensor, which is the frequency dependent transfer function of the electric and magnetic field vectors. The complex elements of the impedance tensor are parameters that provide information on geoelectrical structures. These parameters are the following: apparent resistivity (bulk average resistivity), phase of the impedance; geomagnetic transfer function (induction vector) and dimension indicators (e.g. phase tensor ellipses) which are derived from primary impedances (Wiese, 1962; Swift, 1967; Bibby, 1977; Caldwell et al., 2004; Berdichevsky and Dmitriev, 2010).

During 2013 to 2014, long period MT data were collected at 14 stations (coordinates are listed in Supplementary Table 1) along a ~60 km long NNW–SSE profile in the NGVF (Fig. 1b) with the aim of characterizing the electrical resistivity image of the lithosphere and determining the depth of the LAB. During the measurements, a LEMI-417 acquisition system was applied, in which the time variation of the magnetic field components (H_x, H_y and H_z) were measured by flux-gate magnetometer. The telluric field components E_x and E_y were observed by non-polarized Cu-$CuSO_4$ electrodes using 50 m long electric dipoles. The orientation of the magnetic and telluric sensors was set to principal axis of Earth's magnetic field (NS and EW). The distance between MT stations was 3–5 km depending on topography, location of xenolith-bearing quarries and potential man-made noise areas. In order to eliminate artificial electromagnetic (EM) noise, three instruments were applied simultaneously, which allowed the implementation of remote

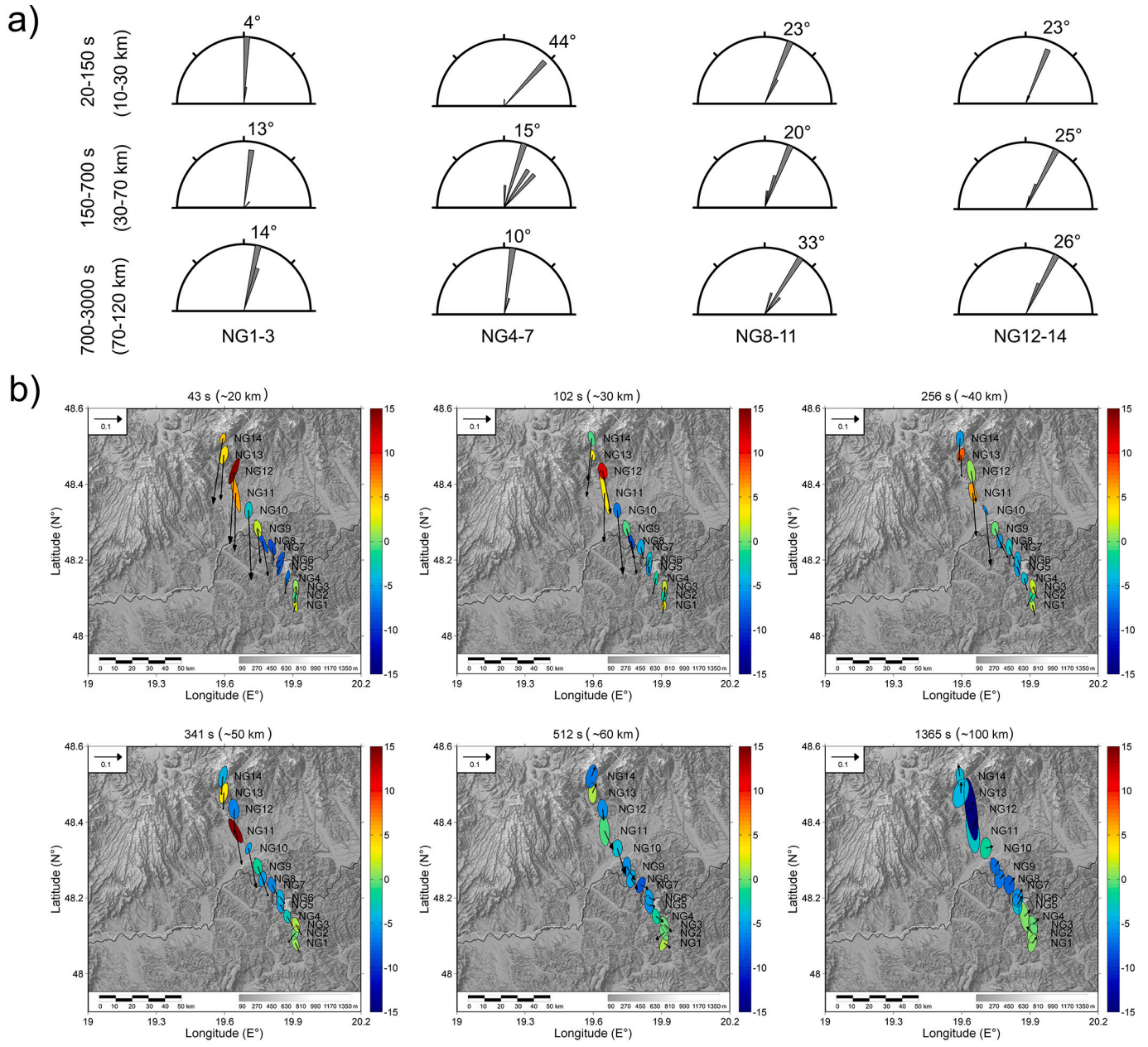

Fig. 3. (a) Rose diagrams of electrical strike directions for crustal (10–30 km), lithospheric mantle (30–70 km) and asthenospheric (70–120 km) depths. (b) Induction vectors and phase tensor ellipses for all MT stations (showing black arrows) at different time periods at estimated depths of 20, 30 and 40 km, respectively. Depth estimations are based on the averages of different approaches including Skin depth (Cagniard, 1953), Bostick depth (Bostick and Smith, 1962), modified Bostick depth (Martí i Castells, 2006) and Schmucker depth (Schmucker, 1973).

reference approach (Varentsov et al., 2003). The average recording time was approximately 4–5 days at a single station. The electromagnetic time variations were collected at a rate of 4 Hz, where the available period range was approximately between 10 and 10000 s. The time series were processed using robust single-site, and in two cases (NG12 and NG13 stations; Fig. 1b), remote reference processing code to estimate MT transfer functions (Egbert and Booker, 1986; Egbert and Livelybrooks, 1996). Strong artificial electromagnetic noise was observed in case of some MT stations (NG9, NG11, NG12; Fig. 1b), which were situated in the vicinity of settlements. Occasionally, telluric wires were damaged by animals, which restricted the length of the appropriate time series. In order to reach the LAB depth and construct broadband MT sounding curves, the recorded effective EM time variation lasted minimum 36 h without any disturbances. Selected MT sounding curves are shown on Fig. 2. The transfer function of the MT stations was estimated using on average 48 frequency bands and 0.95 coherency condition for electric and magnetic field components.

4. Electrical strike directions, induction vectors and phase tensor ellipses

Before the 1-D and 2-D inversions, we calculated the electrical strike directions, induction vectors and phase tensor ellipses too.

The electrical strike directions were calculated by tensor decomposition following the method of Groom and Bailey (1989). The results were grouped by 3–4 MT stations and illustrated on rose diagrams (Fig. 3a). The calculated directions point predominantly to NNE (Fig. 3a). Significant variation was only observed in the group of NG4-NG7 stations, where the crust shows N44°E, whereas the mantle has around N10°E–N15°E electrical strike. In the northern part of the MT profile (NG12–NG14), minimal diversity was observed in the electrical strike of different depth ranges (N23°E–N26°E) (Fig. 3a). The established geoelectric strike direction is N20°E.

Induction vectors were calculated from geomagnetic data based on the considerations of Wiese (1962). The induction vectors provide information on the position and extent of potential low resistivity (<10 Ωm) bodies. The length of the induction vector defines the electrical resistivity, whereas its direction points towards the low electrical resistivity anomalies. At periods between 43–341 s (~20–50 km), the induction vectors of some MT stations located at central and northern part of the profile (NG8–NG14) point to the south and have great length (Fig. 3b). The long vectors disappear at greater depth (>50 km), and their direction changes dominantly to SE and NE at ~60 km and ~100 km, respectively (Fig. 3b).

The magnetotelluric phase tensor ellipse (Caldwell et al., 2004) is a tool to obtain information on the dimensionality of the regional electrical structures by galvanic distortion. It is defined by the inverse tangent ratio between the imaginary and real parts of the magnetotelluric tensor (Weaver et al., 2000). The phase tensor ellipses refer to the dimension of electrical structures by ellipticity and β skew angle (represented by colors) of the ellipses. In the northern part of the profile (NG10–NG14), phase tensor ellipses have strong ellipticity and high β skew angle (>0) for periods 43–341 s (Fig. 3b). In the same MT stations, the ellipticity remains strong, but the β skew angles turn to a negative value at periods 512–1365 s. In MT stations NG4–NG9, the phase tensor ellipses are moderately variable, whereas those at the southernmost three MT stations (NG1–NG3) are quite homogenous for the entire section (Fig. 3b).

5. 1-D and 2-D inversion results

Reduction of the MT data was carried out using different inversion models including layered 1-D (Geosystem, 2000), automatic Occam's 1-D (Constable et al., 1987) and 2-D inversions (Rodi and Mackie, 2001). The static shift and galvanic distortion were eliminated by Groom-Bailey decomposition (Groom and Bailey, 1989). Both the layered and the automatic Occam's 1-D inversions (Fig. 4a) were calculated applying the invariant apparent resistivity.

The layered 1-D inversion gives the electrical resistivity and thickness of layers in all MT stations (Fig. 4a). The appropriateness of the inversion was verified by the low RMS (root mean square) misfit value (average RMS = 0.1355) (Supplementary Fig. 1). The presented values are in nRMS (normalized RMS). The layers south of the NG12 station are characterized by low electrical resistivities (<20 Ωm) (Fig. 4a). The only exception is the depth range of ~10–25 km, where electrical resistivity values are dominantly over 40 Ωm (Fig. 4a). In the northern part of the MT profile (NG12–NG14), high electrical resistivity values (>100 Ωm) are the most frequent (Fig. 4a). For determining the asthenospheric indication, only those layers were taken into account where the electrical resistivity dropped by 5–25 Ωm below 50 km. According to these criteria, the LAB depth is placed between 54–70 km south of the NG12 station (Fig. 4a; Table 1). Further asthenospheric indication was observed beneath the three northernmost stations (NG12–NG14) with an estimated LAB depth of >100 km (Table 1; Supplementary Fig. 1).

Based on the automatic Occam's 1-D inversion results (Fig. 4a), the electrical resistivity is uniformly low (<10 Ωm) in the upper part of the crust (top 5 km). Beneath the central part of the section (NG9-NG10 stations) an anomaly with low electrical resistivity (<10 Ωm) was detected at lower crustal depth (10–20 km). In contrast, beneath the southern and the northern part of the section, highly resistive bodies (>500 Ωm) were found in the lower crust. The rest of the lower crust has an average of ~100 Ωm electrical resistivity. Below the crust, a conductive anomaly was detected with a low resistivity (<5 Ωm) at ~20–60 km depth range in the central part of the section (NG6–NG11 stations) (Fig. 4a). The horizontal extension of this anomaly is more than 30 km. The indication of the asthenosphere at 60–80 km depth is observed in the southern 30 km of the section (Fig. 4a). However, in the rest of the section, the depth of the LAB was impossible to determine (Fig. 4a).

In order to test the results of the 1-D inversions, we carried out 2-D inversion as well. The sounding curves (Fig. 2) were rotated with N20°E based on the electrical strike direction (Fig. 3a). The 2-D inversion was inverted by the non-linear conjugate gradient algorithm of Rodi and Mackie (2001) implemented in WinGLink software. In the modelling, homogeneous half-space approach was applied with 100 Ωm electrical resistivity as an average value based on the result of the 1-D inversion (Fig. 4a). The elevation of the stations was also taken into account. In order to achieve the final 2-D model, a few tests (>10) were carried out to obtain the best smoothing parameters of error floor, electrical resistivity range, regularization parameter, static shift correction and weighting function. The 2-D inversions were carried out using bimodal inversion (Transversal Electric (TE) + Transversal Magnetic (TM)), where the conjugate data of the vertical magnetic component (H_z) was taken into account. Error floor of 5% for both TE and TM modes were applied. The static shift correction was automatically used and the RMS was minimized by 100 iterations. Data errors were set to 10% (apparent resistivity) and 5% (phase) (Supplementary Fig. 2). For equal weighting of apparent resistivity and phase in the inversion, the error of phase was selected as the half of that for apparent resistivity. Error floors of apparent resistivity and phase were both 5%, where phase error is introduced in % equivalent to apparent resistivity error (i.e., 1% apparent resistivity error is equivalent to a 0.29 degree absolute error in phase). The error floor for induction vector was set to 0.1 absolute magnitude value. Since the average amplitude of induction vector magnitude is ~0.6 and the standard deviation is ~0.3, we determined the error floor values to be 0.1 (~15%). The Supplementary Fig. 3 shows the fitting of the induction vectors in 2-D inversion.

The best solution of the inversion is shown on Fig. 4b. The shallow part of the section (<20 km) shows several elongated (5–10 km) anomalies with high (>100 Ωm) and low (<10 Ωm) resistivity values (Fig. 4b). Below the Moho a low resistivity (<2 Ωm) structure has been revealed in the depth range of 30–60 km beneath stations NG5-NG9

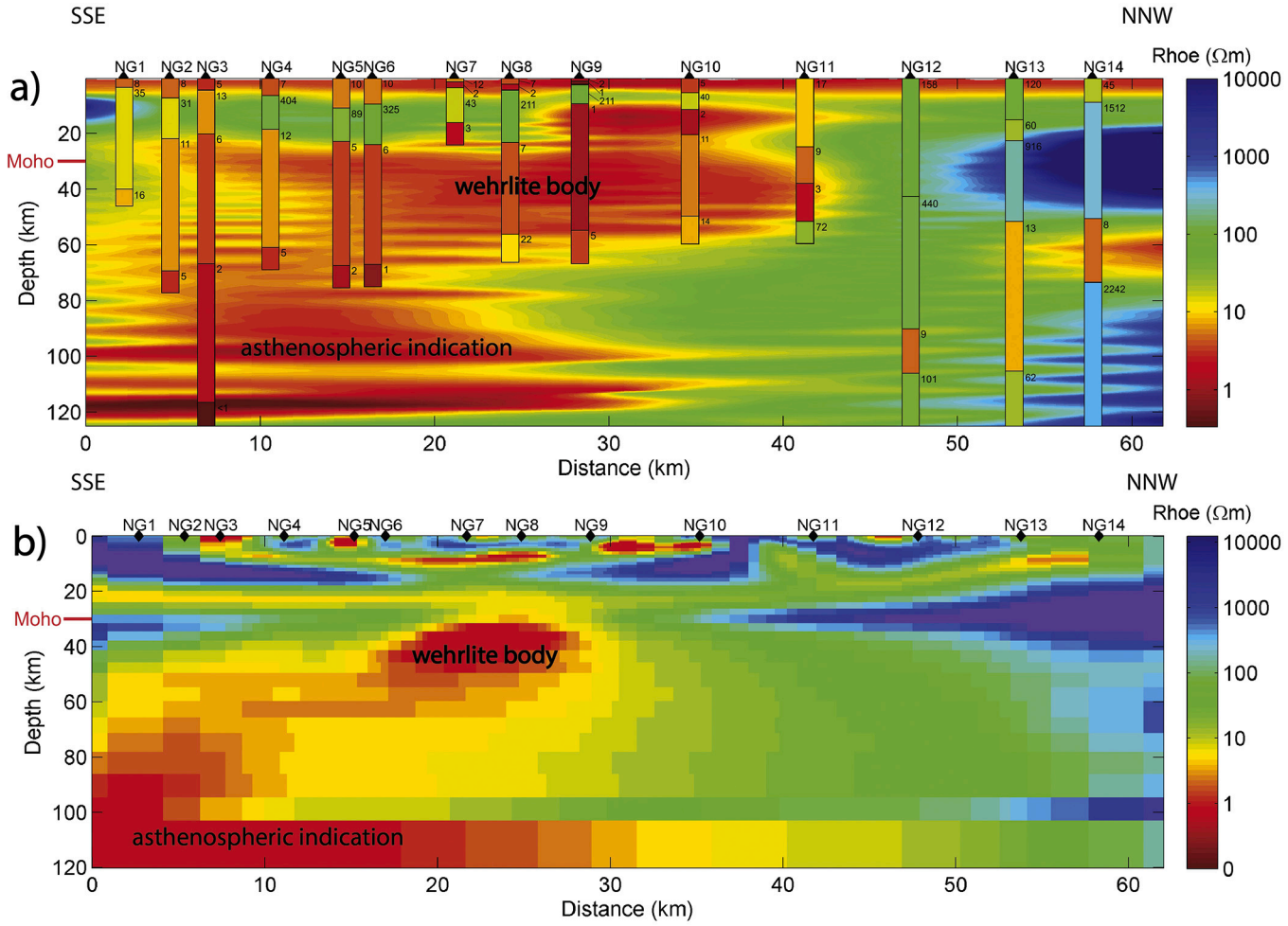

Fig. 4. (a) Layered 1-D (columns) and automatic Occam's 1-D inversion models of the MT profile. (b) 2-D inversion model of the MT profile. The static shift and galvanic distortion were eliminated by Groom-Bailey decomposition (Groom and Bailey, 1989). The Moho depth is based on Horváth et al. (2006) and Klébesz et al. (2015).

Table 1
List of the MT stations, with the estimated depth of lithosphere-asthenosphere boundary (LAB) using the 1-D layered inversion (Geosystem, 2000). In some stations (NG1, NG7, NG8, NG10, NG11) results were invalid and are thus not shown. Results of the NG13 and NG14 MT stations are unrealistic and were not taken into account.

MT station	LAB depth (km)
NG1	–
NG2	70
NG3	67
NG4	61
NG5	68
NG6	67
NG7	–
NG8	–
NG9	54
NG10	–
NG11	–
NG12	106
NG13	169
NG14	159

(Fig. 4b), with a horizontal extension of ~15 km. In the southern part of the section (beneath stations NG1–NG9), indication of the asthenosphere with low electrical resistivity (~1 Ωm) appears at the depth of ~80 km (Fig. 4b).

6. Expected electrical resistivity in the lithospheric mantle

We carried out estimations on the electrical resistivity of the rock forming mantle silicates (olivine, orthopyroxene, clinopyroxene) and calculated bulk rocks. As first approach, the effect of fluids/melts were avoided, and only the solid wall rock was considered. We used the excel worksheet modified after Kovács et al. (2018) (Supplementary Table 2) for the calculations. This estimation follows the methodology specified in Fullea (2017). We applied the first parameterization (PC1) (Fullea, 2017 and references therein) in the third term of the equation describing the conductivity of mantle minerals (Supplementary Table 2). Further details are described in Kovács et al. (2018).

In order to calculate the electrical resistivity values for NGVF xenoliths, the characteristic petrographic and geochemical data of the local mantle are needed in addition to the experimentally derived parameters (e.g., activation enthalpies, pre-exponential terms). The 'water' content of the nominally anhydrous minerals (NAMs), which refers to hydrogen incorporated in the crystal lattice as hydroxyl and commonly expressed as H_2O, is probably the most important factor in electrical resistivity (Wang et al., 2006; Dai and Karato, 2009; Yoshino et al., 2009; Poe et al., 2010; Yang et al., 2011; Novella et al., 2017). The clinopyroxene, orthopyroxene and olivine have 'water' contents in a decreasing amount in mantle (Bell and Rossman, 1992; Ingrin and Skogby, 2000; Demouchy

and Bolfan-Casanova, 2016; Peslier et al., 2017).

In the NGVF, clinopyroxenes have lower 'water' content (0.5–481 with an average of 132 ppm) in lherzolites than in the strongly metasomatized wehrlites (21–894 with an average of 302 ppm) (Patkó et al., 2019). Among clinopyroxenes in wehrlite xenoliths, dry (21–464 with an average of 140 ppm) and wet (202–894 with an average of 481 ppm) grain populations were distinguished based on their water 'contents' (Patkó et al., 2019). The 'water' content of the orthopyroxenes is variable in lherzolites (1–147 with an average of 31 ppm) (Patkó et al., 2019). Note that 'water' data of orthopyroxenes is not available for wehrlites and certain lherzolites. The 'water' content of the lherzolitic olivines is usually below detection limit. Similarly, there is no detectable 'water in wehrlitic olivines either (Patkó et al., 2019). The low 'water' content of NAMs is most likely because of pre-, syn- and post-entrapment hydrogen loss (Patkó et al., 2019). The reason why clinopyroxene was affected the least and olivine the most is the different hydrogen diffusion speed in these minerals (e.g. Tian et al., 2017 and references therein). In xenoliths where the 'water' data of orthopyroxene or olivine was not detected, we made estimations on the original hydrogen concentration. Thus, the analyzed 'water' content of clinopyroxenes together with the partition coefficient of hydrogen between clinopyroxene and other silicates were applied ($D^{cpx/opx} = 2.3$; Pintér et al., 2015; $D^{cpx/ol} = 10$; Xia et al., 2019). Sometimes the estimated 'water' contents for olivines resulted in higher values than concentrations measured in orthopyroxenes, which is unrealistic. Thus, in such cases the 'water' content of the orthopyroxenes was calculated as well from clinopyroxene data. All measured and calculated 'water' contents are listed in Supplementary Table 3.

Modal compositions, the X_{Fe} ($X_{Fe} = 1 - Mg\#/100$) ratio of the silicates and equilibration temperatures are taken from Liptai et al. (2017) and Patkó et al. (2020a) for lherzolites and wehrlites, respectively (Supplementary Table 3). The pressure at the origin of the xenoliths is hard to estimate for spinel facies xenoliths. The best approach is to use the alkaline basalt province geotherm (Jones et al., 1983) and the equilibration temperatures (based on the Ca-in-opx thermometer of Nimis and Grütter (2010) modified after the thermometer of Brey and Köhler (1990); $T_{Ca\text{-}in\text{-}opx\ by\ NG10}$), which allows an estimation for the pressure (Supplementary Table 3).

The calculated electrical resistivity values are listed in Table 2. We omitted lherzolite NMM0318 because of its extremely high electrical resistivity (>5000 Ωm for all silicates, respectively) most likely due to its extremely low 'water' concentration (Supplementary Table 3). The calculated electrical resistivity has similarly wide ranges in lherzolitic olivines (74–998 with an average of 314 Ωm) and orthopyroxenes (78–1532 with an average of 364 Ωm) (Fig. 5a). In contrast, the electrical resistivity of clinopyroxenes in lherzolites has a narrower range with lower values (8–589 with an average of 92 Ωm). We calculated the electrical resistivity of the wet and the dry grains of wehrlites separately (Table 2). The electrical resistivity in the order of decreasing values is the following in wet grains: olivine (72–106 with an average of 90 Ωm), orthopyroxene (58–86 with an average of 73 Ωm) and clinopyroxene (6–14 with an average of 10 Ωm) (Fig. 5a). The same values are higher in dry grains: olivine (148–538 with an average of 293 Ωm), orthopyroxene (119–450 with an average of 243 Ωm) and clinopyroxene (21–253 with an average of 101 Ωm) (Fig. 5a). The bulk rock electrical resistivity is higher in lherzolites (48–913 with an average of 273 Ωm) compared to that in wehrlites calculated using dry (94–406 with an average of 208 Ωm) and wet grains (47–63 with an average of 55 Ωm) (Fig. 5b). In case of the lherzolite bulk rock, electrical resistivities are different based on spatial distribution. There are high average electrical resistivities in the northern (NPY–520 Ωm; NMS–418 Ωm) as well as in the southern-central (NMC–539 Ωm; NMM–317 Ωm; NME–320 Ωm) and southern (NBN–381 Ωm) NGVF localities (Fig. 1b). The only exception is Jelšovec locality in the north (NJS–97 Ωm), which has low average electrical resistivity likewise in the northern-central sites (NFL–188 Ωm; NTB–138 Ωm; NFK–160 Ωm; NFR–123 Ωm) (Fig. 1b).

7. Discussion

7.1. Geological interpretation of MT data

7.1.1. Crust

Even though the position of the Moho cannot be detected by MT (Fig. 4), it is reasonable to divide and interpret the observed structures based on their location relative to the known Moho. The crustal thickness beneath the study area is well constrained, the Moho stretches at 25–30 km in depth (Horváth et al., 2006; Klébesz et al., 2015).

The northern part of the profile (NG12–NG14 stations) is situated on a terrain where the Veporicum outcrops on the surface (Fig. 1b), therefore the resistive (45–150 Ωm) layers that appear both in 1-D and 2-D inversion models were interpreted to represent the metamorphic complexes of the Veporicum crystalline units (Fig. 4). Comparing our results with the MT data obtained along nearby profiles (Bezák et al., 2014, 2015, 2020), it is reasonable to assume that this resistive body is part of the Veporic granitoid complex.

In the southern and central parts of the profile (NG1–NG11 stations), the crust is characterized by relatively low electrical resistivity structures (<80 Ωm) on 1-D inversion image (Fig. 4a). The shallow, less resistive (<10 Ωm) structures are associated with Neogene to Quaternary sediments underlain by Eocene to Early Miocene sedimentary rocks and possibly Gemeric metasediments containing graphitic shales (Bezák et al., 2015 and references therein). The deeper parts of the crust are likely composed of Veporic crystalline rocks, i.e. sub-thrust of the Gemerides (Bezák et al., 2015), which are also known in several boreholes in adjacent areas (Koroknai et al., 2001). However, the resolution of the sounding is not enough to differentiate among Veporic units. Between stations NG9 and NG10, (and below stations NG2 to NG8 to some extent,) the body with low electrical resistivity (<10 Ωm) may be physically and/or genetically connected to the low resistivity crustal structures observed in the 2T profile of Bezák et al., 2015. The authors interpreted these structures to be the result of prior intensive Neogene tectonic and volcanic processes associated with conductive fluid migration and hydrothermal ore mineralization.

The 2-D inversion results (Fig. 4b) reveal several low (<10 Ωm) and high (>100 Ωm) resistivity bodies in the crustal level of the southern and central parts of the profile (NG1–NG11 stations). This higher resolution of 2-D than 1-D inversions for the crust is due to the application of TE+TM modes and geomagnetic data (H_z). The heterogeneous crust and the lack of drilling cores also make the interpretation of the MT data challenging. The low resistivity anomaly found beneath the NG9 and NG10 MT stations is also observed on the 2-D inversion image, with lateral extension stretching below stations NG8-NG6 (Fig. 4b). The previously described interpretation of fluid migration linking to tectonic and volcanic processes (Bezák et al., 2015) can be feasible here as well.

The electrical strike directions and phase tensor ellipses in crustal depth can be also explained by local crustal geology. Electrical strike directions are varying between N4°E–N44°E (Fig. 3a). This is roughly perpendicular to the SW-NE strike direction of tectonic unit boundaries in the Carpathian thrust system (e.g. Plašienka et al., 1997). The reason of the strong ellipticities and high β skew angles in the northern part of the profile is attributed to the presence of Veporic units with 3D electrical structures (Fig. 3b).

7.1.2. Lithospheric mantle

The sub-Moho part of the profile is characterized by similar electrical resistivity distribution both on 1-D and 2-D inversion images (Fig. 4). Generally, the lithospheric mantle has electrical resistivity <100 Ωm. The only exception is below the two northwestern most stations (NG13–NG14), where the high electrical resistivity (>100 Ωm) determined for the crust extends towards the lithospheric mantle as well (Fig. 4). These two stations are located north of the surface appearance of the alkali basaltic volcanic products (Fig. 1b). Thus, it is reasonable to deduce that the generally higher electrical resistivity in the lithospheric

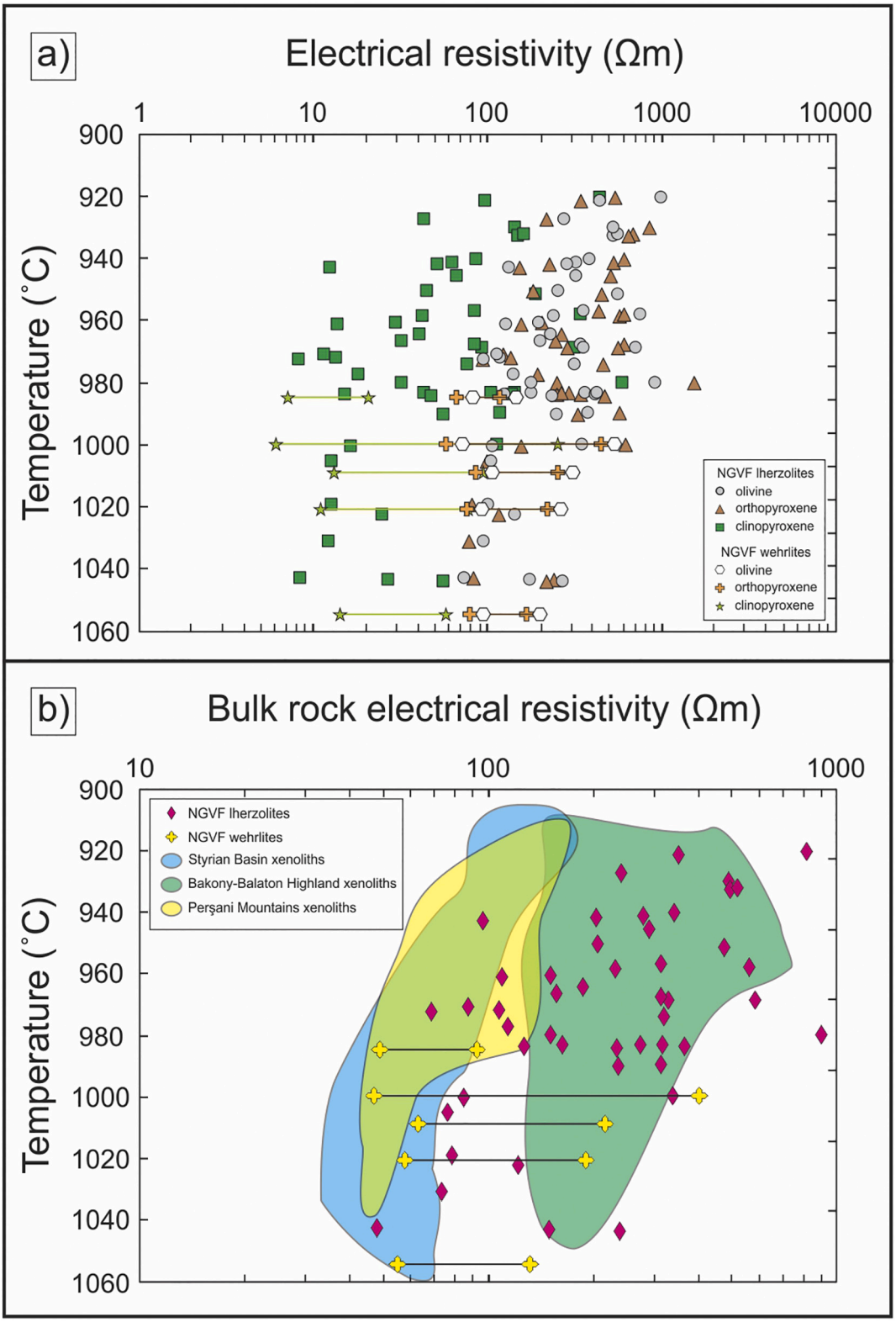

Fig. 5. (a) Electrical resistivity of the rock forming minerals (olivine, clinopyroxene, orthopyroxene) of Nógrád-Gömör lherzolite and wehrlite xenoliths in function of equilibration temperature. The results of dry and wet wehrlitic grains from the same xenoliths are connected with solid lines showing wet grains by lower electrical resistivity values. (b) Bulk rock electrical resistivities of lherzolite and wehrlite xenoliths in function of equilibration temperature. Reference data were calculated based on Aradi et al. (2017) for Styrian Basin, Liptai et al. (2021) for Bakony-Balaton Highland and Falus et al. (2008) and Lange et al. (2019) for Perşani Mountains. The results of the same wehrlites using dry and wet grains, respectively, are connected with solid lines showing wet grains by lower electrical resistivity values.

Table 2
Electrical resistivity results of the rock forming silicates and bulk rocks of the Nógrád-Gömör wehrlite xenoliths. The values were calculated using the excel worksheet of Supplementary Table 2 modified after Kovács et al. (2018). Abbreviations: ol - olivine, opx - orthopyroxene, cpx - clinopyroxene, bulk - calculated whole rock.
Electrical resistivity results of the rock forming silicates and bulk rocks of the Nógrád-Gömör wehrlite xenoliths. The values were calculated using the excel worksheet of Supplementary Table 2 modified after Kovács et al. (2018). Abbreviations: ol - olivine, opx - orthopyroxene, cpx - clinopyroxene, bulk - calculated whole rock.

	Xenolith		Electrical resistivity (Ωm)			
			ol	opx	cpx	bulk
Lherzolite series	NPY1301		557	449	189	477
	NPY1314		759	606	343	564
	NMS1302A		277	218	43	242
	NMS1304		998	540	442	828
	NMS1305		286	227	51	206
	NMS1308		527	842	143	493
	NMS1310		314	460	77	321
	NJS1302		197	206	30	153
	NJS1304		129	156	14	110
	NJS1306		74	83	8	48
	NJS1307		105	98	13	77
	NFL1302		202	246	32	158
	NFL1305		114	124	12	89
	NFL1315A		356	288	94	330
	NFL1316		242	567	42	232
	NFL1324		249	328	56	239
	NFL1327		100	82	13	79
	NFL1329		232	264	41	189
	NTB0306		257	184	45	207
	NTB0307		132	151	13	97
	NTB1124		179	247	32	152
	NTB1116		175	242	27	150
	NTB1122		107	157	17	86
	NFK0301		126	249	15	128
	NFK1108		178	254	43	164
	NFK1115		268	216	56	239
	NFK1123		118	135	13	108
	NFR0306		95	78	12	75
	NFR0307		94	94	8	69
	NFR0309		142	192	18	115
	NFR1107		233	466	48	235
	NFR1109		143	117	25	122
	NMC1301		352	620	113	340
	NMC1309		376	570	118	315
	NMC1322		707	563	319	589
	NMC1336A		909	1532	589	913
	NMM0318		5043	5249	16913	5782
	NMM1115		354	436	84	315
	NMM1126		426	264	143	319
	NME0528		417	339	138	369
	NME1116		362	293	106	276
	NME1122		341	602	85	316
	NBN0302A		554	681	163	522
	NBN0305		530	644	149	497
	NBN0311		440	345	97	355
	NBN0316		383	600	87	344
	NBN0319		321	525	63	279
	NBN0321		324	512	66	291
Wehrlite series	NFR1117A	dry grains	148	119	21	94
		wet grains	83	67	7	49
	NFR1119B	dry grains	538	450	253	406
		wet grains	72	58	6	47
	NMC1302B	dry grains	310	256	95	217
		wet grains	106	86	13	63
	NMC1343	dry grains	267	220	78	192
		wet grains	93	76	11	58
	NMM1114	dry grains	202	169	58	133
		wet grains	95	79	14	55

mantle under these stations is related to the lacking effect of volcanism on the mantle. The melt migration in association with the alkali basaltic volcanic activity may have pervasively metasomatized mantle volumes along the melt migration pathways and decreased the electrical resistivity. The extension of Veporic granitoid units below the local Moho as an explanation for high electrical resistivity is definitely less likely.

Beneath the central part of the NGVF, directly below Moho, a low resistivity body (<10 Ωm) appears both in 1-D and 2-D inversion images (Fig. 4). The anomaly extends till the depth of ~60 km (Fig. 4), which is also supported by the disappearing long induction vectors at greater depths (Fig. 3b). The spatial distribution of wehrlite xenoliths correlates well with this observed anomaly (Patkó et al., 2020a). To answer the question whether wehrlite bodies can be the reason for the anomaly, the results of electrical resistivity calculations can be examined and compared with those of the lherzolites, which represent the precursor mantle rocks of the wehrlites (Patkó et al., 2020a).

7.1.2.1. Low resistivity anomaly in the mirror of wehrlite and lherzolite characteristics. The electrical resistivity of a peridotite depends on several factors. Numerous studies in the past two decades revealed that the greater the 'water' content of nominally anhydrous minerals (NAMs), the lower their electrical resistivity (Wang et al., 2006; Dai and Karato, 2009; Yoshino et al., 2009; Poe et al., 2010; Yang et al., 2011; Jones et al., 2012; Novella et al., 2017). The presence of wet clinopyroxenes with high 'water' contents (>202 ppm) in the NGVF wehrlites causes high 'water' concentrations in the bulk rock (>62 ppm), resulting in wehrlites having lower electrical resistivity than 'dryer' wall rock lherzolites (Patkó et al., 2019). Other factors like modal composition, geochemical characteristics and pressure-temperature conditions all have an impact on the electrical resistivity, but their effect is less significant (Selway, 2014; Fullea, 2017). According to Karato and Wang (2013), the electrical resistivity of NAMs is the following in decreasing order: olivine, orthopyroxene, clinopyroxene, which is true for the NGVF as well (Fig. 5a). It follows that the elevated clinopyroxene content in wehrlites (~21 vol.%; Patkó et al., 2020a) compared to the lherzolites (~9 vol.%; Liptai et al., 2017) results in lower bulk electrical resistivity. The greater iron concentration in the mineral phases, and consequently in bulk rocks, leads to lower electrical resistivity as well (Hinze et al., 1981; Seifert et al., 1982; Omura et al., 1989; Yoshino et al., 2012). Since the wehrlitization leads to Fe enrichment, wehrlites have higher Fe contents than lherzolites (Patkó et al., 2020a). According to experiments conducted with multi-anvil apparatus, increasing pressure and temperature considerably reduces the electrical resistivity in olivines (Xu et al., 2000; Yoshino et al., 2012), whereas in pyroxenes, this effect is minimal (Dai et al., 2006). There is a small difference in the pressure-temperature conditions of the NGVF wehrlites (985–1055 with an average of 1014 °C using $T_{Ca\text{-}in\text{-}opx\ by\ NG10}$ and 1.3–1.6 GPa; Patkó et al., 2020a) and lherzolites (921–1044 with an average of 973 °C using $T_{Ca\text{-}in\text{-}opx\ by\ NG10}$ and 1.2–1.5 GPa; Liptai et al., 2017), which may have a weak additional role in the lower electrical resistivity of the former.

As a conclusion, all parameters suggest lower electrical resistivity in wehrlite than in lherzolite xenoliths. Therefore, the wehrlitization must have considerable effect on the electrical resistivity in the mantle volume affected by metasomatism. This is further supported by the estimated electrical resistivity of bulk rocks, which are lower for wehrlites (average values are 55 and 208 Ωm based on wet and dry grains, respectively) than lherzolites (with an average of 273 Ωm) (Table 2). Although the modal proportion of wet and dry rock forming minerals is unknown in the wehrlites, their bulk electrical resistivity is likely no higher than 150 Ωm.

Note that electrical resistivity difference exists not only between the wehrlite and the lherzolites xenolith, but also appears among the lherzolite samples. The northern-central localities (NFL, NTB, NFK, NFR; Fig. 1b) are characterized with lower average electrical resistivities (<200 Ωm; Table 2). Similarly, the northern locality of Jelšovec has low

average electrical resistivity (NJS–97 Ωm). In contrast, the rest of the localities (NPY, NMS, NMC, NMM, NME, NBN; Fig. 1b) all have higher average electrical resistivities (>300 Ωm; Table 2). This can be explained by the 'water' content variability in the lherzolites (Supplementary Table 3). Jelšovec is the only locality, where the xenoliths are in pyroclastic rocks, so their higher 'water' content is possibly related to their fast cooling on surface (Patkó et al., 2019). Note however that water concentrations are only conservative estimates, even in Jelšovec locality, because 'water' loss cannot be excluded. Therefore, electrical resistivity values are maximum estimates, which can be lower.

7.1.2.2. Possible role of fluids/melts in low electrical resistivity. The estimated electrical resistivity of wehrlites is lower than those of the lherzolites (Fig. 5b), however, not as low as measured by MT (Fig. 4). Thus, the metasomatic alteration solely cannot account for the observed anomaly. Graphite films on grain boundaries (Mareschal et al., 1995; Glover, 1996; Santos et al., 2002; Jones et al., 2003) or the presence of interconnected fluids/melt (Desissa et al., 2013; Johnson et al., 2016; Ebinger et al., 2017; Magee et al., 2018; Selway et al., 2019, 2020) can further decrease the electrical resistivity, and may clarify the observed discrepancy. Graphite was not found in the studied xenoliths, hence its effect on lowering the electrical resistivity is unlikely. In contrast, the presence of fluids and melts are proved by fluid (Konečná, 1990; Szabó and Bodnar, 1996, 1998) and silicate melt inclusion (Szabó et al., 1996; Patkó et al., 2018; Liptai et al., 2020) studies. Furthermore, the wehrlite (Patkó et al., 2020a) and cumulate formation (Kovács et al., 2004; Zajacz et al., 2007) suggest intense fluid and melt migration, especially beneath the central part of the NGVF.

A recent study (Patkó et al., 2020b), on volumetric ratio and spatial distribution of solid phases and vesicles in metasomatized wehrlites from NGVF using X-ray microtomography revealed presence of 2–6 vol.% glass with no relationship to the host basalt, forming an interconnected network along grain boundaries. The glass is accompanied by 0.4–1.5 vol.% of vesicles, which represents pores after the loss of formerly dissolved gas phases (Patkó et al., 2020b). This suggests that at the time of the entrapment of xenoliths in the host basalt, silicate melt was present in the upper mantle, which solidified into glass due to cooling most likely on the surface. The last phase of alkali basalt volcanism in the NGVF ceased about 0.3 Ma ago in the central part of the NGVF (Hurai et al., 2013). Since the longevity of such systems may span on the magnitude of 100 ka (Bourdon et al., 1994), some fluids or melts may still exist in the upper mantle beneath the central NGVF, which can lead to a decrease in the electrical resistivity. Note that experimental runs reveal that even ~0.5 vol.% of basaltic melt can form interconnected network and thus lower the electrical resistivity (Laumonier et al., 2017). The potential presence of melts beneath NGVF coincides with the implication of Kovács et al. (2020), who concluded that partial melts could be still present in the asthenosphere of CPR and can infiltrate to the lithospheric mantle along deep deformation zones.

If we accept the assumption that partial melt could still pond underneath the NGVF, a question raises regarding its amount. To answer this question, a numerical modelling was carried out based on the methodology in Sifré et al. (2014). Note that estimated electrical resistivity of dry and wet wehrlites (Table 2) as input parameter of melt-free metasomatic products was used. We examined the effect of increasing amount of melt (0–10 vol.%) containing various quantities of dissolved CO_2 (0–2 wt.%) on electrical resistivity. The H_2O content of the melt was calculated for each wehrlite xenolith using the bulk 'water' content of the wehrlites (Supplementary Table 4) and the partition coefficient of H_2O between silicate melt and the mineral constituents (olivine, orthopyroxene, clinopyroxene) according to the formulae of Hirschmann et al. (2009). The results reveal 0.01–0.2 wt.% and 0.2–0.5 wt.% water contents for silicate melts being in equilibrium with dry and wet wehrlites, respectively (Supplementary Table 4). The detailed description of the modelling can be found in Supplementary Text 1.

The results of the modelling show similar images irrespectively to the different starting wehrlites (Fig. 6). The major inference is that the higher the melt fraction in the peridotite, the lower the electrical resistivity. The only exception is a field characterized by melt fraction greater than ~1 vol.%, accompanied with low CO_2 content (<0.6 wt.%). In case of small melt fraction (<1 vol.%), the amount of CO_2 in the melt does not influence the electrical resistivity. In contrast, when the melt fraction exceeds 1 vol.%, the higher the CO_2 content in the melt, the lower the electrical resistivity.

The X-ray microtomography done by Patkó et al. (2020b) revealed 2–6 vol.% interconnected glass in wehrlites in the NGVF. This suggests that the melt fraction reasonable to consider is equal to this range. The CO_2 concentration of the melt can also be constrained with the use of silicate melt inclusions (SMIs), which are representative melt drops. According to Szabó et al. (1996), the CO_2 content of SMIs has an average of 1.55 wt.%. Based on the study of Patkó et al. (2020a), such intermediate melts can be formed during wehrlitization as a result of orthopyroxene dissolution. Similar average CO_2 concentration of wehrlitization related SMIs (1.68 wt.%) was calculated using the data of Liptai et al. (2020). On the modelled diagrams (Fig. 6), melt fractions of 2–5 vol.% and CO_2 contents of 1.5–1.7 wt.% suggest electrical resistivities of <1 Ωm. It is likely that the 2–6 vol.% melt fraction was only valid for the interval of active volcanism, which could have ceased 300 ka ago (Hurai et al., 2013). Note however that even as little as 1 vol.% of melt can reduce the electrical resistivity to ~2.5 Ωm, and 0.5 vol.% melt fraction leads to ~5 Ωm electrical resistivity.

The conclusion drawn from the xenoliths and the electrical resistivity modelling is that the anomaly measured with MT is likely explained by wehrlite bodies with <2 vol.% interconnected silicate melt. Thus, it is reasonable to assume that the MT measurements reveal the distribution of wehrlitization. Based on this conclusion, the metasomatism affected a large volume of the mantle (~30 km long and ~15 km thick), which suggests that migration of the metasomatic melt along grain boundaries was quite extensive. In addition, it is plausible to assume that ponding, interconnected network of silicate melt is still present in the wehrlite-rich lithospheric mantle.

7.2. The depth of the lithosphere-asthenosphere boundary (LAB)

Long period MT data are widely applied for LAB depth determination because of the contrast between the more resistive lithospheric mantle (generally few tens to hundreds Ωm) and the less resistive asthenosphere (generally 1–25 Ωm) (e.g. Korja, 2007). In this study, the depth of the LAB is defined by using the layered 1-D inversion model, however, the automatic Occam's 1-D and the 2-D inversion models also suggest asthenospheric indications at somewhat greater depth (Fig. 4). Considering that the research area is situated in the transition zone between the extended Pannonian Basin and the Carpathian orogen (Fig. 1a), a change in the depth of the LAB it is expectable. The result is ~65 km in the southern and central (NG2–NG11), and 105–170 km in the northern part (NG12–NG14) of the profile (Table 1; Supplementary Fig. 1). However, such an extreme variation in the LAB depth within a few tens of km is rather unlikely.

We compared our results with published LAB depth data implemented with various approaches. According to the review of Ádám and Wesztergom (2001), the LAB is located at a 75–85 km depth range beneath the NGVF based on MT measurements. Geissler et al. (2010) and Klébesz et al. (2015) both used the receiver function approach and estimated a similar LAB depth, 74 km and 65 (±10) km, respectively. The estimation of Tašárová et al. (2009) using 3D gravity modeling reveal somewhat deeper LAB position (~80–100 km). An even thicker lithosphere of ~100–120 km was suggested by Bielik et al. (2010) using integrated 2D modeling of gravity, geoid, topography, and surface heat flow data.

Based on these results, the ~65 km and even the 106 km (Table 1) compares relatively well with literature. The reason we get ambiguous

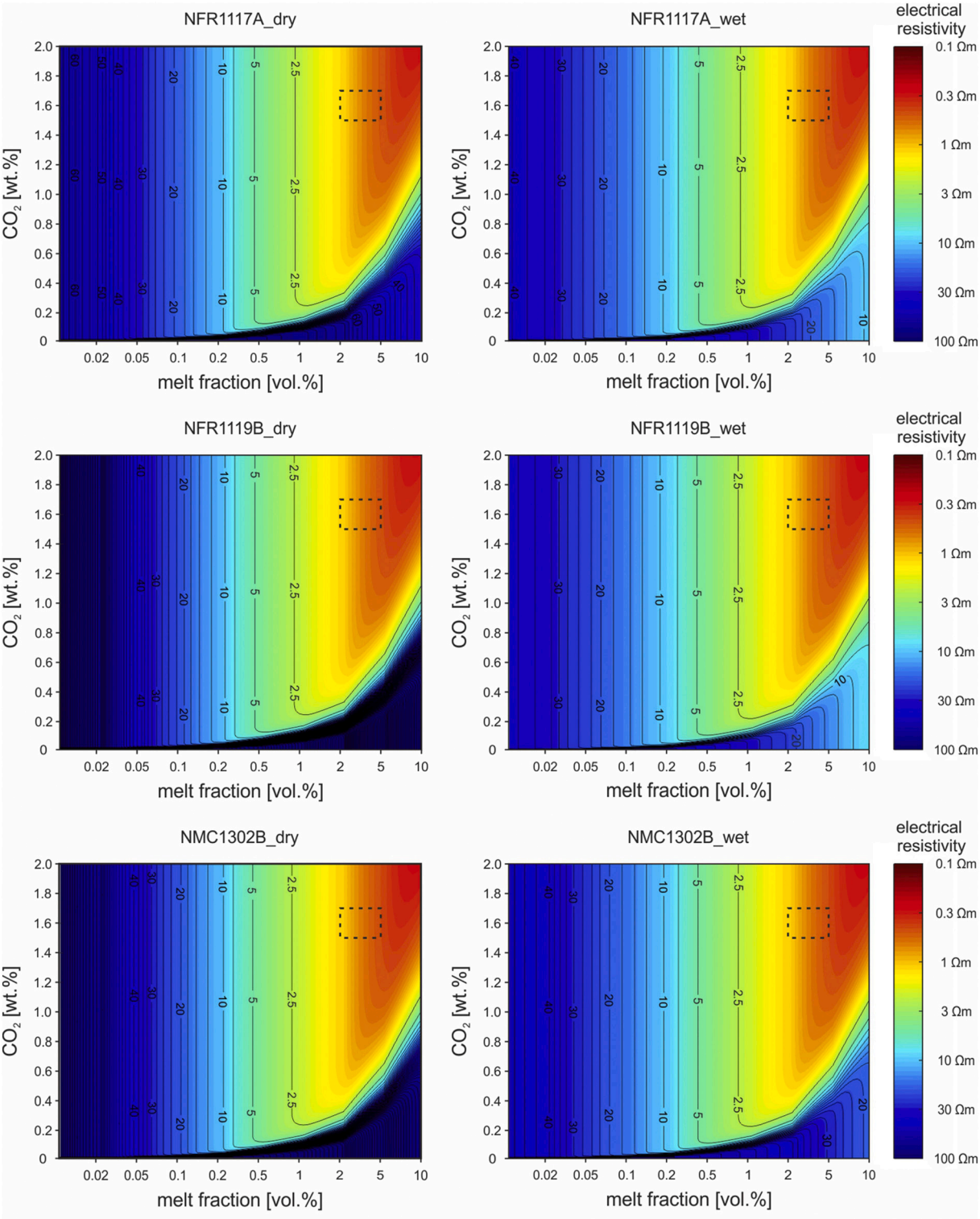

Fig. 6. Modelled electrical resistivity of wehrlite xenoliths (NFR1117A, NFR1119B, NMC1302B, NMC1343, NMM1114) containing different amounts of melt (melt fraction) and variable dissolved CO_2 concentrations. The boxes with dashed lines mark the field proposed for the NGVF (2–5 vol.% melt, 1.4–1.6 wt.% CO_2). The possible melt fraction range is approximated by the modal presence of silicate glass in wehrlite xenoliths (Patkó et al., 2020b), whereas the probable CO_2 content of the melt is defined by silicate melt inclusions from NGVF xenoliths (Szabó et al., 1996; Liptai et al., 2020).

results for some MT station regarding the LAB, especially from the central part of the NGVF (e.g. NG7, NG8, NG10, NG11; Table 1), can be the low resistivity body underneath this section of the MT profile (Fig. 4). The electric charges, which cause electromagnetic induction, may be connected stronger to the conductive body located at shallower depths than the asthenospheric indication at greater depth (galvanic distortion effect; Chave and Smith, 1994).

The depths estimated beneath the northernmost stations

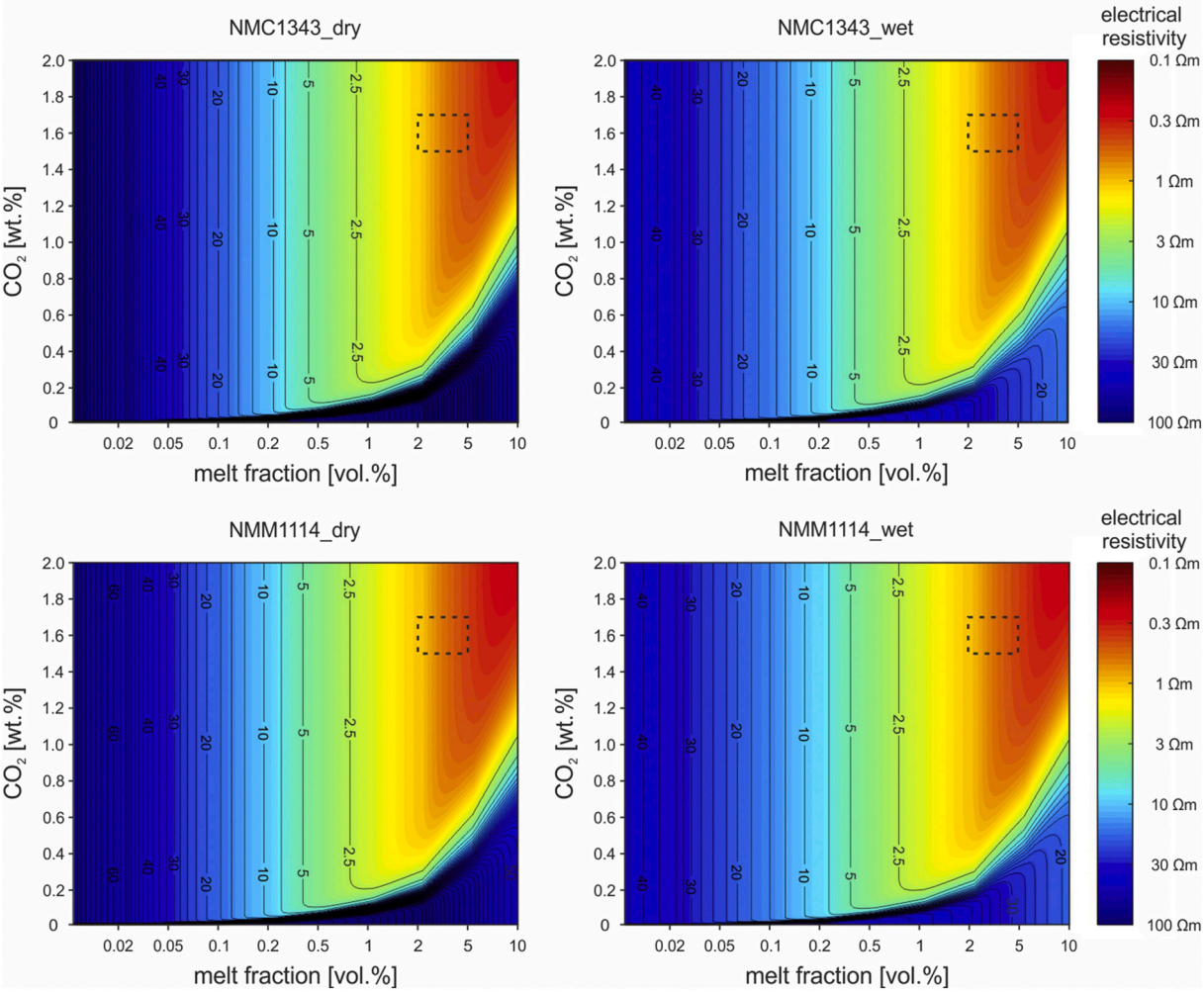

Fig. 6. (*continued*).

(NG13–NG14 stations, >150 km) are significantly deeper than any published estimates. These data are unrealistic and likely caused by the shading effect of an extensive low resistivity body in the crust beneath these stations (Fig. 4). Such low resistivity anomaly can act as an insulator and cause uncertainty in determining electrical resistivity of greater depth below the anomaly.

As a conclusion, the LAB is at ~60–70 km and ~80–100 km in the southern and northern part of the MT section, respectively (Table 1). This suggests a gradual LAB deepening towards the north.

7.3. Hurbanovo-Diósjenő Line and its possible role in melt migration

The 1-D and 2-D inversions reveal that the intensively metasomatized mantle volume is restricted to the central part of the NGVF (Fig. 4). This is also the area, where long (>5 km) lava flows appear on surface in the form of Medves Plateau and Babi Hill (Fig. 1b). The question is raised, what can be the reason of this focused melt upwelling? Tectonic control is a possible explanation for this observation. The Hurbanovo-Diósjenő Lineament and the Rapovce Fault is assumed to be located beneath the study area (Fig. 7), however, their exact position is uncertain. The WSW-ENE directed Hurbanovo-Diósjenő Lineament represents a boundary between the highly-tectonized Central Western Carpathians and the barely deformed Transdanubian Range and Bükk units (Haas et al., 2014). The formation of this lineament started in Oligocene along with Paleogene basins in the northern CPR (Tari et al., 1993; Kováč et al., 2016). Further activities followed until the Pliocene-Quaternary boundary based on sedimentological interpretations (Klučiar et al., 2016). The lineament is covered by several hundred meters thick Neogene to Quaternary sediments and volcanic rocks. Furthermore, the Hurbanovo-Diósjenő Lineament is not a discrete line but rather a few km wide dislocation zone (Balla, 1989). All these make the determination of the exact location challenging. Thus, borehole-based geological data (Balla, 1989) and geophysical methods such as geomagnetism (Haáz and Komáromy, 1967), gravity (Balla, 1989) and MT (Ádám et al., 2003) were invoked earlier. Based on these, the lineament is assumed beneath the Medves Plateau (Fig. 1b).

To test this proposed location, the MT results can be of use. Tectonic zones are often characterized by low electrical resistivity values due to smaller average grain size (ten Grotenhuis et al., 2004) and presence of fluids/melts that migrate through (Brasse et al., 2002; Wannamaker et al., 2002). Furthermore, Pommier et al. (2018) revealed that tectonic zones are conduction paths in the shear direction. There are several low resistivity bodies (<10 Ωm) between the NG2–NG10 MT stations in the crust (<20 km depth) based on the 2-D inversion results (Fig. 4b). These MT stations cover the central part of the NGVF including the Medves Plateau and Babi Hill along a span of ~20–25 km (Fig. 1b). MT results beneath other part of the Hurbanovo-Diósjenő Lineament 40–50 km to the west of the NGVF reveal similar low electrical resistivities (<20 Ωm) with lower crustal penetration depths (~15 km) (Ádám et al., 2003). Therefore, this zone with low electrical resistivity values can be linked to diffuse tectonic structures, which confirms the presumption of Balla (1989) on a several km wide tectonic zone. Several faults including the Rapovce fault were distinguished by other MT studies targeted at the crust beneath the southern part of the Central Western Carpathians

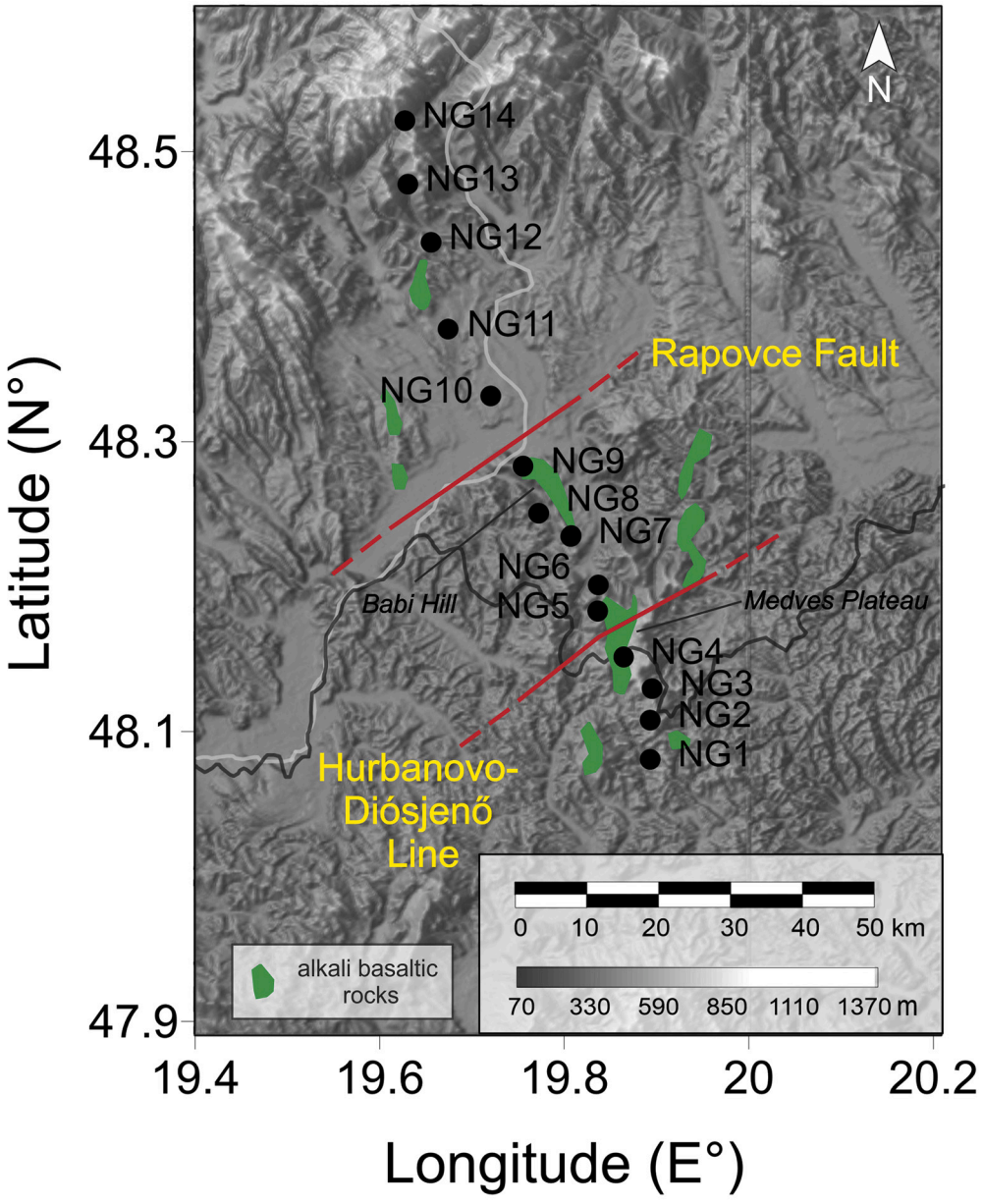

Fig. 7. Possible position of the Hurbanovo-Diósjenő Lineament and Rapovce fault in the NGVF based on the MT measurements and the conclusion of prior studies (Balla, 1989; Bezák et al., 2015, 2020).

(Bezák et al., 2014, 2015, 2020). Comparing these prior sections with our measurements, the Rapovce fault is likely situated beneath the northern edge of the Babi Hill (Fig. 7) between stations NG9–NG10, where low resistivity zones in the crust appear according to the 2-D inversion model (Fig. 4b). Bezák et al. (2014, 2015, 2020) did not identify the Hurbanovo-Diósjenő Lineament, which is to the south of the Rapovce fault and was likely out of the research area of those studies. The Hurbanovo-Diósjenő Lineament may account for the low electrical resistivities beneath the Medves Plateau between stations NG4-NG5 (Fig. 4b). However, we cannot exclude that low electrical resistivities are linked to petrographic features. For example, graphitic shales and schists were found in some drilling cores reaching the Veporic and Gemeric units beneath the Cenozoic formations (Kőrössy, 2004). However, these wells aiming to reveal the hydrocarbon potential never reached depths greater than 2 km (Kőrössy, 2004). According to Bezák et al. (2015), graphitic rocks are restricted to the shallower crust (<5 km), hence cannot be responsible for low electrical resistivity in the lower crust.

Another question regarding the Hurbanovo-Diósjenő dislocation zone and Rapovce fault is their possible penetration depths. According to the 2D-inversion image (Fig. 4b) beneath the NG2–NG10 MT stations, the low electrical resistivity zones are deep-rooted (reaching 20 km depth). This suggests that at least some of the fractures belonging to the dislocation zone reach the lower crust. Even more, these low resistivity volumes in the crust seem to be connected to the low resistivity anomaly situated beneath the Moho (Fig. 4).

This raises the possibility that these tectonic zones may crosscut not just the crust, but they extend even deeper in the lithospheric mantle. To investigate this possibility further, we summarized the results of previous studies on deformation patterns of the NGVF upper mantle (Liptai et al., 2013, 2019; Klébesz et al., 2015). According to Liptai et al. (2019), most xenoliths have A-type orthorhombic crystal preferred orientation (CPO) symmetry in the central part of the NGVF, whereas it barely appears in the northern and southern parts. Orthorhombic CPO symmetry

develops under simple shear (Tommasi et al., 1999), which is an indicator of movements along faults. The CPO strength is quantified by the J-index (Bunge, 1982), which show the highest average value for olivines ($J_{ol} = 3.47$) in the central part of the NGVF (Liptai et al., 2019). Thus, the upper mantle is most deformed beneath the central part of the NGVF. Furthermore, vertical foliation is assumed in the upper mantle based on seismic properties (Liptai et al., 2019) and SKS splitting results (Klébesz et al., 2015). This vertical foliation and deformation features could be produced by strike-slip movements between the southern and northern parts of the NGVF along the central zone bound by the Rapovce and Hurbanovo-Diósjenő Lines. The deformation could be also enhanced by the NE-SW compression in the tectonic inversion stage (Kovács et al., 2020). These deformation zones form paths for the basaltic melts which eventually also lead to the pervasive metasomatism of the lithospheric mantle beneath central region.

As a conclusion, the Hurbanovo-Diósjenő Line is regarded as a steep and deep-reaching tectonic zone, which crosscuts the entire lithosphere beneath central part of the NGVF (Fig. 7). In the lower crust it likely connects to a more deformed upper mantle volume with vertical foliation. This section is an excellent channel for melts. This focused melt migration explains the concentrated appearance of extensive metasomatism in the mantle (Patkó et al., 2020a), cumulate formation around the Moho (Kovács et al., 2004; Zajacz et al., 2007) and basalt flows on the surface (Konečný et al., 1995a) in the central part of the NGVF. Moreover, the deep-lying wehrlitic body may explain the major gravity and magnetic anomalies along the Hurbanovo-Diósjenő Line (Haáz and Komáromy, 1967; Balla, 1989).

8. Concluding remarks

1. Long period MT data were collected at 14 stations along a ~50 km long NNW-SSE profile in the NGVF. As a result, the electrical resistivity distribution of the entire lithosphere was defined beneath the volcanic field. The crustal segment of the profile has variable electrical resistivity indicating heterogeneous composition. Below the Moho, the most characteristic structure is a low resistivity anomaly (<10 Ωm) at approx.? 30–60 km depth under the central part of the NGVF. The depth of the LAB is between approx.? 60–70 km in the southern, Pannonian basin part of the profile, and reaches 100 km towards the Western-Carpathians in the north.
2. The location of the low resistivity anomaly in mantle coincides with the distribution of surface localities of wehrlite xenoliths bearing alkali basalts. Previous studies from the NGVF concluded that the wehrlites were formed as a result of intensive interaction between a metasomatic agent and the peridotite wall rock. Thus, the low resistivity anomaly is most likely linked to a petrographically and geochemically altered mantle volume (i.e. a massive wehrlite body).
3. According to our model calculation, the electrical resistivity of the wehrlites (~132 Ωm) is lower than the non-metasomatized lherzolites (~273 Ωm) from the same localities, indicating that the metasomatism led to electrical resistivity decrease. We demonstrated that even ~2–3 vol.% of interconnected melt is enough to obtain electrical resistivities of <1 Ωm in wehrlites. The presence of such and even higher amount of interconnected melt in the intergranular space of wehrlites at the time of xenolith entrapment is in agreement with the modal composition of glass revealed by X-ray microtomography analyses. The MT data suggest that small amounts of melt are possibly still present beneath the NGVF.
4. The reason why the intensive magma upwelling was concentrated on the central part of the NGVF is most likely tectonic. The Hurbanovo-Diósjenő Line, which is a tectonic zone possibly strikes across the lithosphere beneath the central NGVF and is responsible for the focused appearance of extensive metasomatism in the mantle, cumulate formation around the Moho and massive basalt flows on the surface. This indicates that tectonic lines on the surface can crosscut the entire lithosphere in the deep providing a link a between deep and surface processes.

Supplementary data to this article can be found online at https://doi.org/10.1016/j.gloplacha.2020.103389.

Declaration of Competing Interest

The authors declare that they have no known competing financial interests or personal relationships that could have appeared to influence the work reported in this paper.

Acknowledgements

The authors dedicate this paper to the memory of Prof. Frank Horváth, who always intended to combine geological and geophysical knowledge. For this, the entire Earth Science community owes thanks to him.

The authors acknowledge Csaba Molnár for his help with MT measurements in the field and László Szarka for his contribution in MT methodology. This research was supported by the TAMOP-4.2.2.C–11/1/KONV-2012-0015 (Earth-system) project sponsored by the European Social Fund. The project was further financed by a Lendület Research Grant to the MTA CSFK Lendület Pannon LitH_2Oscope Research Group (LP-2018/5) and the NKFIH K128122 grant to the Topo-Transylvania community. This work was completed with the support of the ELTE Institutional Excellence Program (1783-3/2018/FEKUTSRAT) managed by the Hungarian Ministry of Human Capacities to L. Patkó and Cs. Szabó. L. Patkó and T. P. Lange were also supported by the GINOP-2.3.2-15-2016-00009 research program. A. Novak was sponsored by the János Bolyai Scholarship of the Hungarian Academy of Sciences (BO/00795/11/10). This is the 104th publication of the Lithosphere Fluid Research Lab (LRG) collaboration with the GGI.

References

Geosystem, 2000. Integrated Geophysical Interpretation Software for Windows 95/98/NT, WINGLINKTM version 2.73., User's Guide.

Martí i Castells, A., 2006. Magnetotelluric Investigation of Geoelectrical Dimensionality and Study of the Central Betic Crustal Structure. Ph.D. thesis. Universitat de Barcelona, p. 307.

Swift, C.M., 1967. A Magnetotelluric Investigation of an Electrical Conductivity Anomaly in the Southwestern United States. Ph.D. Thesis. Massachusetts Institute of Technology, p. 223.

Ádám, A., Wesztergom, V., 2001. An attempt to map the depth of the electrical asthenosphere by deep magnetotelluric measurements in the Pannonian Basin (Hungary). Acta Geol. Hung. 44 (167-192).

Ádám, A., Novák, A., Szarka, L., Wesztergom, V., 2003. The magnetotelluric (MT) investigation of the Diósjenő dislocation belt. Acta Geodaet. Geophys. Hung. 38 (3), 305–326. https://doi.org/10.1556/AGeod.38.2003.3.2.

Ádám, A., Szarka, L., Novák, A., Wesztergom, V., 2017. Key results on deep electrical conductivity anomalies in the Pannonian Basin (PB), and their geodynamic aspects. Acta Geodaet. Geophys. 52 (2), 205–228. https://doi.org/10.1007/s40328-016-0192-2.

Aiken, C.L., Ander, M.E., 1981. A regional strategy for geothermal exploration with emphasis on gravity and magnetotellurics. J. Volcanol. Geotherm. Res. 9 (1), 1–27. https://doi.org/10.1016/0377-0273(81)90011-1.

Aradi, L.E., Hidas, K., Kovács, I.J., Tommasi, A., Klébesz, R., Garrido, C.J., Szabó, C., 2017. Fluid-Enhanced Annealing in the Subcontinental Lithospheric Mantle Beneath the Westernmost Margin of the Carpathian-Pannonian Extensional Basin System. Tectonics 36 (12), 2987–3011. https://doi.org/10.1002/2017TC004702.

Balla, Z., 1984. The Carpathian loop and Pannonian Basin: a kinematic analysis. Geophysical Transactions 30, 313–355.

Balla, Z., 1989. Reevaluation of the Diósjenő dislocation zone (*in Hungarian*). In: Annual Report of the Eötvös Loránd Geophysical Institute of Hungary for 1987, pp. 45–57.

Balogh, K., Mihaliková, A., Vass, D., 1981. Radiometric dating of basalts in southern and central Slovakia. In: Západné Karpaty: Séria Geológia, 7, pp. 113–126.

Becken, M., Ritter, O., 2012. Magnetotelluric studies at the San Andreas Fault Zone: implications for the role of fluids. Surv. Geophys. 33 (1), 65–105. https://doi.org/10.1007/s10712-011-9144-0.

Bell, D.R., Rossman, G.R., 1992. Water in Earth's mantle: the role of nominally anhydrous minerals. Science 255 (5050), 1391–1397. https://doi.org/10.1126/science.255.5050.1391.

Berdichevsky, M.N., Dmitriev, V.I., 2010. Models and Methods of Magnetotellurics. Springer Science & Business Media, p. 562.

Bezák, V., Pek, J., Vozár, J., Bielik, M., Vozár, J., 2014. Geoelectrical and geological structure of the crust in Western Slovakia. Stud. Geophys. Geod. 58 (3), 473–488. https://doi.org/10.1007/s11200-013-0491-9.

Bezák, V., Pek, J., Majcin, D., Bučová, J., Šoltis, T., Bilčík, D., Klanica, R., 2015. Geological interpretation of magnetotelluric sounding in the southern part of seismic profile 2T (Central Slovakia). Contrib. Geophys. Geodesy. 45 (1), 1–11. https://doi.org/10.1515/congeo-2015-0009.

Bezák, V., Pek, J., Vozár, J., Majcin, D., Bielik, M., Tomek, Č., 2020. Geoelectrically distinct zones in the crust of the Western Carpathians: a consequence of Neogene strike-slip tectonics. Geol. Carpath. 71 (1), 14–23. https://doi.org/10.31577/GeolCarp.71.1.2.

Bibby, H.M., 1977. The apparent resistivity tensor. Geophysics 42 (6), 1258–1261. https://doi.org/10.1190/1.1440791.

Bielik, M., Alasonati-Tašárová, Z., Zeyen, H., Dérerová, J., Afonso, J., Csicsay, K., 2010. Improved geophysical image of the Carpathian-Pannonian basin region. Acta Geodaet. Geophys. Hung. 45 (3), 284–298. https://doi.org/10.1556/AGeod.45.2010.3.3.

Bologna, M.S., Padilha, A.L., Vitorello, Í., Pádua, M.B., 2011. Signatures of continental collisions and magmatic activity in central Brazil as indicated by a magnetotelluric profile across distinct tectonic provinces. Precambrian Res. 185 (1–2), 55–64. https://doi.org/10.1016/j.precamres.2010.12.003.

Bostick, F.X., Smith, H.W., 1962. Investigation of large-scale inhomogeneities in the earth by the magnetotelluric method. Proc. IRE 50 (11), 2339–2346. https://doi.org/10.1109/JRPROC.1962.287961.

Bourdon, B., Zindler, A., Wörner, G., 1994. Evolution of the Laacher See magma chamber: Evidence from SIMS and TIMS measurements of U-Th disequilibria in minerals and glasses. Earth Planet. Sci. Lett. 126 (1-3), 75–90. https://doi.org/10.1016/0012-821X(94)90243-7.

Brasse, H., Lezaeta, P., Rath, V., Schwalenberg, K., Soyer, W., Haak, V., 2002. The Bolivian altiplano conductivity anomaly. J. Geophys. Res. Solid Earth 107 (B5). https://doi.org/10.1029/2001JB000391. EPM-4.

Brey, G.P., Köhler, T., 1990. Geothermobarometry in four-phase lherzolites II. New thermobarometers, and practical assessment of existing thermobarometers. J. Petrol. 31 (6), 1353–1378. https://doi.org/10.1093/petrology/31.6.1353.

Bunge, H.J., 1982. Texture Analysis in Materials Sciences. Buttleworth, London.

Cagniard, L., 1953. Basic theory of the magneto-telluric method of geophysical prospecting. Geophysics 18 (3), 605–635. https://doi.org/10.1190/1.1437915.

Caldwell, T.G., Bibby, H.M., Brown, C., 2004. The magnetotelluric phase tensor. Geophys. J. Int. 158 (2), 457–469. https://doi.org/10.1111/j.1365-246X.2004.02281.x.

Chave, A.D., Smith, J.T., 1994. On electric and magnetic galvanic distortion tensor decompositions. J. Geophys. Res. Solid Earth 99 (B3), 4669–4682. https://doi.org/10.1029/93JB03368.

Constable, S.C., Parker, R.L., Constable, C.G., 1987. Occam's inversion; a practical algorithm for generating smooth models from electromagnetic sounding data. Geophysics 52 (3), 289–300. https://doi.org/10.1190/1.1442303.

Csontos, L., Nagymarosy, A., 1998. The Mid-Hungarian line: a zone of repeated tectonic inversions. Tectonophysics 297 (1-4), 51–71. https://doi.org/10.1016/S0040-1951(98)00163-2.

Csontos, L., Vörös, A., 2004. Mesozoic plate tectonic reconstruction of the Carpathian region. Palaeogeogr. Palaeoclimatol. Palaeoecol. 210 (1), 1–56. https://doi.org/10.1016/j.palaeo.2004.02.033.

Dai, L., Karato, S.I., 2009. Electrical conductivity of orthopyroxene: implications for the water content of the asthenosphere. Proc. Jpn. Acad. Ser. B 85 (10), 466–475. https://doi.org/10.2183/pjab.85.466.

Dai, L., Li, H., Liu, C., Su, G., Shan, S., 2006. Experimental measurement of the electrical conductivity of pyroxenite at high temperature and high pressure under different oxygen fugacities. High Pressure Res. 26 (3), 193–202. https://doi.org/10.1080/08957950600725503.

Demouchy, S., Bolfan-Casanova, N., 2016. Distribution and transport of hydrogen in the lithospheric mantle: A review. Lithos 240, 402–425. https://doi.org/10.1016/j.lithos.2015.11.012.

Desissa, M., Johnson, N.E., Whaler, K.A., Hautot, S., Fisseha, S., Dawes, G.J.K., 2013. A mantle magma reservoir beneath an incipient mid-ocean ridge in Afar, Ethiopia. Nat. Geosci. 6 (10), 861–865. https://doi.org/10.1038/ngeo1925.

Eaton, D.W., Darbyshire, F., Evans, R.L., Grütter, H., Jones, A.G., Yuan, X., 2009. The elusive lithosphere–asthenosphere boundary (LAB) beneath cratons. Lithos 109 (1-2), 1–22. https://doi.org/10.1016/j.lithos.2008.05.009.

Ebinger, C.J., Keir, D., Bastow, I.D., Whaler, K., Hammond, J.O., Ayele, A., Miller, M.S., Tiberi, C., Hautot, S., 2017. Crustal structure of active deformation zones in Africa: implications for global crustal processes. Tectonics 36 (12), 3298–3332. https://doi.org/10.1002/2017TC004526.

Egbert, G.D., Booker, J.R., 1986. Robust estimation of geomagnetic transfer functions. Geophys. J. R. Astron. Soc. 87 (1), 173–194. https://doi.org/10.1111/j.1365-246X.1986.tb04552.x.

Egbert, G.D., Livelybrooks, D.W., 1996. Single station magnetotelluric impedance estimation: Coherence weighting and the regression M-estimate. Geophysics 61 (4), 964–970. https://doi.org/10.1190/1.1444045.

Embey-Isztin, A., Downes, H., James, D.E., Upton, B.G.J., Dobosi, G., Ingram, G.A., Harmon, H.G., Scharbert, H.G., 1993. The petrogenesis of Pliocene alkaline volcanic rocks from the Pannonian Basin, Eastern Central Europe. J. Petrol. 34 (2), 317–343. https://doi.org/10.1093/petrology/34.2.317.

Evans, R.L., Elsenbeck, J., Zhu, J., Abdelsalam, M.G., Sarafian, E., Mutamina, D., Chilongola, F., Atekwana, E.A., Jones, A.G., 2019. Structure of the Lithosphere Beneath the Barotse Basin, Western Zambia, From Magnetotelluric Data. Tectonics 38 (2), 666–686. https://doi.org/10.1029/2018TC005246.

Falus, Gy, Tommasi, A., Ingrin, J., Szabó, Cs, 2008. Deformation and seismic anisotropy of the lithospheric mantle in the southeastern Carpathians inferred from the study of mantle xenoliths. Earth Planet. Sci. Lett. 272 (1-2), 50–64. https://doi.org/10.1016/j.epsl.2008.04.035.

Fodor, L., Csontos, L., Bada, G., Györfi, I., Benkovics, L., 1999. Tertiary tectonic evolution of the Pannonian Basin system and neighbouring orogens: a new synthesis of palaeostress data. Geol. Soc. Lond., Spec. Publ. 156 (1), 295–334. https://doi.org/10.1144/GSL.SP.1999.156.01.15.

Fullea, J., 2017. On joint modelling of electrical conductivity and other geophysical and petrological observables to infer the structure of the lithosphere and underlying upper mantle. Surv. Geophys. 38 (5), 963–1004. https://doi.org/10.1007/s10712-017-9432-4.

Fullea, J., Muller, M.R., Jones, A.G., 2011. Electrical conductivity of continental lithospheric mantle from integrated geophysical and petrological modeling: Application to the Kaapvaal Craton and Rehoboth Terrane, southern Africa. J. Geophys. Res. Solid Earth 116 (B10). https://doi.org/10.1029/2011JB008544.

Geissler, W.H., Sodoudi, F., Kind, R., 2010. Thickness of the central and eastern European lithosphere as seen by S receiver functions. Geophys. J. Int. 181 (2), 604–634. https://doi.org/10.1111/j.1365-246X.2010.04548.x.

Glover, P.W.J., 1996. Graphite and electrical conductivity in the lower continental crust: a review. Phys. Chem. Earth 21 (4), 279–287. https://doi.org/10.1016/S0079-1946(97)00049-9.

Groom, R.W., Bailey, R.C., 1989. Decomposition of magnetotelluric impedance tensors in the presence of local three-dimensional galvanic distortion. J. Geophys. Res. Solid Earth 94 (B2), 1913–1925. https://doi.org/10.1029/JB094iB02p01913.

ten Grotenhuis, S.M., Drury, M.R., Peach, C.J., Spiers, C.J., 2004. Electrical properties of fine-grained olivine: Evidence for grain boundary transport. J. Geophys. Res. Solid Earth 109 (B6). https://doi.org/10.1029/2003JB002799.

Haas, J., Budai, T., Csontos, L., Fodor, L., Konrád, G.Y., Koroknai, B., 2014. Geology of the pre-Cenozoic basement of Hungary. Geological and Geophysical Institute of Hungary, Budapest, pp. 1–71.

Haáz, I., Komáromy, I., 1967. Geomagnetic map of Hungary. A series of 200000, M-34-XXXII. Salgótarján, L-34-I. Tatabánya, L-34-II. Budapest, ELGI, Budapest.

Harangi, Sz., 2001. Neogene to Quaternary volcanism of the Carpathian-Pannonian Region - a review. Acta Geol. Hung. 44 (2-3), 223–258.

Hautot, S., Tarits, P., Whaler, K., Le Gall, B., Tiercelin, J.J., Le Turdu, C., 2000. Deep structure of the Baringo Rift Basin (central Kenya) from three-dimensional magnetotelluric imaging: Implications for rift evolution. J. Geophys. Res. Solid Earth 105 (B10), 23493–23518. https://doi.org/10.1029/2000JB900213.

Hill, G.J., Caldwell, T.G., Heise, W., Chertkoff, D.G., Bibby, H.M., Burgess, M.K., Cull, J. P., Cas, R.A.F., 2009. Distribution of melt beneath Mount St Helens and Mount Adams inferred from magnetotelluric data. Nat. Geosci. 2 (11), 785. https://doi.org/10.1038/ngeo661.

Hinze, E., Will, G., Cemič, L., 1981. Electrical conductivity measurements on synthetic olivines and on olivine, enstatite and diopside from Dreiser Weiher, Eifel (Germany) under defined thermodynamic activities as a function of temperature and pressure. Phys. Earth Planet. Inter. 25 (3), 245–254. https://doi.org/10.1016/0031-9201(81)90068-6.

Hirschmann, M.M., Tenner, T., Aubaud, C., Withers, A.C., 2009. Dehydration melting of nominally anhydrous mantle: The primacy of partitioning. Phys. Earth Planet. Inter. 176 (1–2), 54–68.

Hók, J., Šujan, M., Šipka, F., 2014. Tektonické členenie Západných Karpát - prehľad názorov a nový prístup. Acta Geologica Slovaca 6 (2), 135–143.

Horváth, F., Bada, G., Szafián, P., Tari, G., Ádám, A., Cloetingh, S., 2006. Formation and deformation of the Pannonian Basin: constraints from observational data. Geol. Soc. Lond. Mem. 32 (1), 191–206. https://doi.org/10.1144/GSL.MEM.2006.032.01.11.

Hovorka, D., Fejdi, P., 1980. Spinel peridotite xenoliths in the west Carpathian late Cenozoic alkali basalts and their tectonic significance. Bull. Volcanol. 43 (1), 95. https://doi.org/10.1007/BF02597614.

Hurai, V., Danišík, M., Huraiová, M., Paquette, J.-L., Ádám, A., 2013. Combined U/Pb and (U–Th)/He geochronometry of basalt maars in Western Carpathians: implications for age of intraplate volcanism and origin of zircon metasomatism. Contrib. Mineral. Petrol. 166 (4), 1235–1251. https://doi.org/10.1007/s00410-013-0922-1.

Ingrin, J., Skogby, H., 2000. Hydrogen in nominally anhydrous upper-mantle minerals: concentration levels and implications. Eur. J. Mineral. 12 (3), 543–570. https://doi.org/10.1127/0935-1221/2000/0012-0543.

Johnson, N.E., Whaler, K.A., Hautot, S., Fisseha, S., Desissa, M., Dawes, G.J.K., 2016. Magma imaged magnetotellurically beneath an active and an inactive magmatic segment in Afar, Ethiopia. Geol. Soc. Lond., Spec. Publ. 420 (1), 105–125. https://doi.org/10.1144/SP420.11.

Jones, A.P., Smith, J.V., Dawson, J.B., Hansen, E.C., 1983. Metamorphism, partial melting, and K-metasomatism of garnet-scapolite-kyanite granulite xenoliths from Lashaine, Tanzania. The Journal of Geology 91 (2), 143–165.

Jones, A.G., Lezaeta, P., Ferguson, I.J., Chave, A.D., Evans, R.L., Garcia, X., Spratt, J., 2003. The electrical structure of the Slave craton. Lithos 71 (2–4), 505–527. https://doi.org/10.1016/j.lithos.2003.08.001.

Jones, A.G., Plomerová, J., Korja, T., Sodoudi, F., Spakman, W., 2010. Europe from the bottom up: a statistical examination of the central and northern European lithosphere–asthenosphere boundary from comparing seismological and electromagnetic observations. Lithos 120 (1–2), 14–29. https://doi.org/10.1016/j.lithos.2010.07.013.

Jones, A.G., Fullea, J., Evans, R.L., Muller, M.R., 2012. Water in cratonic lithosphere: Calibrating laboratory-determined models of electrical conductivity of mantle minerals using geophysical and petrological observations. Geochem. Geophys. Geosyst. 13 (6) https://doi.org/10.1029/2012GC004055.

Karato, S.-I., Wang, D., 2013. Electrical conductivity of minerals and rocks. In: Karato, S.-I. (Ed.), Physics and Chemistry of the deep earth. Wiley, Chichester.
Kázmér, M., Kovács, S., 1985. Permian-Palaeogene paleogeography along the eastern part of the Insubric-Periariatic Lineament system: evidence for continental escape of the Bakony-Drauzug Unit. Acta Geol. Hung. 28, 71–84.
Khan, A., Connolly, J.A.D., Olsen, N., 2006. Constraining the composition and thermal state of the mantle beneath Europe from inversion of long-period electromagnetic sounding data. J. Geophys. Res. Solid Earth 111 (B10). https://doi.org/10.1029/2006JB004270.
Klébesz, R., Gráczer, Z., Szanyi, Gy, Liptai, N., Kovács, I., Patkó, L., Pintér, Z., Falus, Gy, Wesztergom, V., Szabó, C., 2015. Constraints on the thickness and seismic properties of the lithosphere in an extensional setting (Nógrád-Gömör Volcanic Field, Northern Pannonian Basin). Acta Geodaet. Geophys. 50 (2), 133–149. https://doi.org/10.1007/s40328-014-0094-0.
Klučiar, T., Kováč, M., Vojtko, R., Rybár, S., Šujan, M., Králiková, S., 2016. The Hurbanovo–Diósjenő Fault: A crustal-scale weakness zone at the boundary between the Central Western Carpathians and Northern Pannonian Domain. Acta Geolog. Slov. 8 (1), 59–70.
Konečná, M., 1990. Fluidné inkluzie a termodynamické podmienky vzniku xenolitov spinelovych lherzolitov v alkalickych bazaltoch kuzného Slovenska. Mineral. Slov. 22 (6), 555–564.
Konečný, P., Konečny, V., Lexa, J., Huraiová, M., 1995a. Mantle xenoliths in alkali basalts of Southern Slovakia. Acta Vulcanol. 7 (2), 241–247.
Konečný, V., Lexa, J., Balogh, K., Konečný, P., 1995b. Alkali basalt volcanism in Southern Slovakia: volcanic forms and time evolution. Acta Vulcanol. 7, 167–172.
Korja, T., 2007. How is the European Lithosphere Imaged by Magnetotellurics? Surv. Geophys. 28 (2), 239–272. https://doi.org/10.1007/s10712-007-9024-9.
Koroknai, B., Horváth, P., Balogh, K., Dunkl, I., 2001. Alpine metamorphic evolution and cooling history of the Veporic basement in northern Hungary: new petrological and geochronological constraints. Int. J. Earth Sci. 90, 740–757. https://doi.org/10.1007/s005310000185.
Kőrössy, L., 2004. Hydrocarbon geology of northern Hungary (Palaeogene basin) (*in Hungarian*). Általános Földtani Szemle 28, 9–120.
Kováč, M., Plašienka, D., Soták, J., Vojtko, R., Oszczypko, N., Less, G., Ćosović, V., Fügenschuh, B., Králiková, S., 2016. Paleogene palaeogeography and basin evolution of the Western Carpathians, Northern Pannonian domain and adjoining areas. Glob. Planet. Chang. 140, 9–27. https://doi.org/10.1016/j.gloplacha.2016.03.007.
Kovács, I., Zajacz, Z., Cs, Szabó, 2004. Type-II xenoliths and related metasomatism from the Nógrád-Gömör Volcanic Field, Carpathian-Pannonian region (northern Hungary–southern Slovakia). Tectonophysics 393 (1–4), 139–161. https://doi.org/10.1016/j.tecto.2004.07.032.
Kovács, I.J., Patkó, L., Gy, Falus, Aradi, L.E., Gy, Szanyi, Gráczer, Z., Cs, Szabó, 2018. Upper mantle xenoliths as sources of geophysical information: the Perşani Mts. area as a case study. Acta Geodaet. Geophys. 53 (3), 415–438. https://doi.org/10.1007/s40328-018-0231-2.
Kovács, I., Patkó, L., Liptai, N., Lange, T.P., Taracsák, Z., Cloetingh, S.A.P.L., Török, K., Király, E., Karátson, D., Biró, T., Kiss, J., Pálos, Zs, Aradi, L.E., Falus, Gy, Hidas, K., Berkesi, M., Koptev, A., Novák, A., Wesztergom, V., Fancsik, T., Szabó, Cs, 2020. The role of water and compression in the genesis of alkaline basalts: Inferences from the Carpathian-Pannonian region. Lithos 354, 105323. https://doi.org/10.1016/j.lithos.2019.105323.
Lange, T.P., Szabó, C., Liptai, N., Patkó, L., Gelencsér, O., Aradi, L.E., Kovács, I.J., 2019. A földköpeny reológiai kutatása: mennyiségi Fourier transzformációs infravörös spektrometria alkalmazása egy Persány hegységi xenolit példáján. Földtani Közlöny 149 (3, 4), 233. https://doi.org/10.23928/foldt.kozl.2019.149.3.233.
Laumonier, M., Farla, R., Frost, D.J., Katsura, T., Marquardt, K., Bouvier, A.S., Baumgartner, L.P., 2017. Experimental determination of melt interconnectivity and electrical conductivity in the upper mantle. Earth Planet. Sci. Lett. 463, 286–297. https://doi.org/10.1016/j.epsl.2017.01.037.
Lexa, J., Bezák, V., Elečko, M., Mello, J., Polák, M., Potfaj, M., Vozár, J., 2000. Geologická mapa Západných Karpát a priľahlých území – Geological Map of Western Carpathians and Adjacent Areas 1:500000. Geological Survey of Slovak Republic, Bratislava.
Lexa, J., Seghedi, I., Németh, K., Szakács, A., Konečný, V., Pécskay, Z., Fülöp, A., Kovacs, M., 2010. Neogene-Quaternary volcanic forms in the Carpathian-Pannonian Region: a review. Open Geosci. 2 (3), 207–270. https://doi.org/10.2478/v10085-010-0024-5.
Liptai, N., Jung, H., Park, M., Szabó, C., 2013. Olivinorientáció-vizsgálatok a nógrád–gömöri vulkáni terület déli részéről származó felsőköpeny eredetű xenolitokban. Földtani Közlöny 143 (4), 371–382.
Liptai, N., Patkó, L., Kovács, I.J., Hidas, K., Zs, Pintér, Jeffries, T., Zajacz, Z., O'Reilly, S. Y., Griffin, W.L., Pearson, N.J., Cs, Szabó, 2017. Multiple metasomatism beneath the Nógrád–Gömör Volcanic Field (Northern Pannonian Basin) revealed by upper mantle peridotite xenoliths. J. Petrol. 58 (6), 1107–1144. https://doi.org/10.1093/petrology/egx048.
Liptai, N., Hidas, K., Tommasi, A., Patkó, L., Kovács, I.J., Griffin, W.L., O'Reilly, S.Y., Pearson, N.J., Szabó, Cs, 2019. Lateral and vertical heterogeneity in the lithospheric mantle at the northern margin of the Pannonian Basin reconstructed from peridotite xenolith microstructures. J. Geophys. Res. Solid Earth 124 (7), 6315–6336. https://doi.org/10.1029/2018JB016582.
Liptai, N., Berkesi, M., Patkó, L., Bodnar, R.J., O'Reilly, S.Y., Griffin, W.L., Szabó, Cs, 2020. Characterization of the metasomatizing agent in the upper mantle beneath the northern Pannonian Basin based on Raman imaging, FIB-SEM and LA-ICP-MS analyses of silicate melt inclusions in spinel peridotite. Am. Mineral. https://doi.org/10.2138/am-2019-7292 (in press).
Liptai, N., Lange, T.P., Patkó, L., Pintér, Zs., Berkesi, M., Aradi, L.E., Szabó, Cs., Kovács, I. J., 2021. Effect of 'water' on the rheology of the lithospheric mantle in young extensional basin systems as shown by xenoliths from the Carpathian-Pannonian region. Global Planet. Chang. 196, 103364. https://doi.org/10.1016/j.gloplacha.2020.103364.
Magee, C., Stevenson, C.T., Ebmeier, S.K., Keir, D., Hammond, J.O., Gottsmann, J.H., Whaler, K.A., Schofield, N., Jackson, C.A.-L., Petronis, M.S., O'Driscoll, B., Morgan, J., Cruden, A., Vollgger, S.A., Dering, G., Micklethwaite, S., Jackson, M.D., 2018. Magma plumbing systems: a geophysical perspective. J. Petrol. 59 (6), 1217–1251. https://doi.org/10.1093/petrology/egy064.
Mareschal, M., Kellett, R.L., Kurtz, R.D., Ludden, J.N., Ji, S., Bailey, R.C., 1995. Archaean cratonic roots, mantle shear zones and deep electrical anisotropy. Nature 375 (6527), 134–137. https://doi.org/10.1038/375134a0.
Muller, M.R., Jones, A.G., Evans, R.L., Grütter, H.S., Hatton, C., Garcia, X., Hamilton, M. P., Miensopust, M.P., Cole, P., Ngwisanyi, T., Hutchins, D., Fourie, C.J., Jelsma, H.A., Evans, S.F., Aravanis, T., Pettit, W., Webb, S.J., Wasborg, J., SAMTEX Team, 2009. Lithospheric structure, evolution and diamond prospectivity of the Rehoboth Terrane and western Kaapvaal Craton, southern Africa: constraints from broadband magnetotellurics. Lithos 112, 93–105. https://doi.org/10.1016/j.lithos.2009.06.023.
Nimis, P., Grütter, H., 2010. Internally consistent geothermometers for garnet peridotites and pyroxenites. Contrib. Mineral. Petrol. 159 (3), 411–427. https://doi.org/10.1007/s00410-009-0455-9.
Novella, D., Jacobsen, B., Weber, P.K., Tyburczy, J.A., Ryerson, F.J., Du Frane, W.L., 2017. Hydrogen self-diffusion in single crystal olivine and electrical conductivity of the Earth's mantle. Sci. Rep. 7 (1), 5344. https://doi.org/10.1038/s41598-017-05113-6.
Omura, K., Kurita, K., Kumazawa, M., 1989. Experimental study of pressure dependence of electrical conductivity of olivine at high temperatures. Phys. Earth Planet. Inter. 57 (3-4), 291–303. https://doi.org/10.1016/0031-9201(89)90118-0.
Orange, A.S., 1989. Magnetotelluric exploration for hydrocarbons. Proc. IEEE 77 (2), 287–317. https://doi.org/10.1109/5.18627.
Patkó, L., Liptai, N., Aradi, L.E., Bodnar, R.J., Sendula, E., Kovács, I.J., Klébesz, R., Szabó, C., 2018. Deciphering mantle metasomatism using silicate melt inclusions beneath the Nógrád-Gömör Volcanic Field (Northern Pannonian Basin). EGU General Assembly, 8-13 April, Vienna (Austria). Geophys. Res. Abstr. 20, EGU2018–785.
Patkó, L., Liptai, N., Kovács, I.J., Aradi, L., Xia, Q.-K., Ingrin, J., Mihály, J., O'Reilly, S., Griffin, W.L., Wesztergom, V., Cs, Szabó, 2019. Extremely low structural hydroxyl contents in upper mantle xenoliths from the Nógrád-Gömör Volcanic Field (northern Pannonian Basin): geodynamic implications and the role of post-eruptive re-equilibration. Chem. Geol. 507, 23–41. https://doi.org/10.1016/j.chemgeo.2018.12.017.
Patkó, L., Liptai, N., Aradi, L.E., Klébesz, R., Sendula, E., Bodnar, R.J., Kovács, I.J., Hidas, K., Cesare, B., Novák, A., Trásy, B., Cs, Szabó, 2020a. Metasomatism-induced wehrlite formation in the upper mantle beneath the Nógrád-Gömör Volcanic Field (Northern Pannonian Basin): evidence from xenoliths. Geosci. Front. 11 (3), 934–964. https://doi.org/10.1016/j.gsf.2019.09.012.
Patkó, L., Créon, L., Kovács, Z., Liptai, N., Rosenberg, E., Szabó, Cs., 2020b. Three-dimensional distribution of glass and vesicles in metasomatized xenoliths: a micro-CT case study from Nógrád-Gömör Volcanic Field (Northern Pannonian Basin). Geol. Carpath. 71 (5), 418–423. https://doi.org/10.31577/GeolCarp.71.5.3.
Peslier, A.H., Schönbächler, M., Busemann, H., Karato, S.I., 2017. Water in the Earth's interior: distribution and origin. Space Sci. Rev. 212 (1–2), 743–810. https://doi.org/10.1007/s11214-017-0387-z.
Pintér, Zs, Patkó, L., Djoukam, J.F.T., Kovács, I., Tchouankoue, J.P., Gy, Falus, Konc, Z., Tommasi, A., Barou, F., Mihály, J., Németh, Cs., Jeffries, T., 2015. Characterization of the sub-continental lithospheric mantle beneath the Cameroon volcanic line inferred from alkaline basalt hosted peridotite xenoliths from Barombi Mbo and Nyos Lakes. J. Afr. Earth Sci. 111, 170–193. https://doi.org/10.1016/j.jafrearsci.2015.07.006.
Plašienka, D., Grecula, P., Putiš, M., Kováč, M., Hovorka, D., 1997. Evolution and structure of the Western Carpathians: an overview. In: Geological Evolution of the Western Carpathians, pp. 1–24.
Poe, B.T., Romano, C., Nestola, F., Smyth, J.R., 2010. Electrical conductivity anisotropy of dry and hydrous olivine at 8 GPa. Phys. Earth Planet. Inter. 181 (3–4), 103–111. https://doi.org/10.1016/j.pepi.2010.05.003.
Pommier, A., Kohlstedt, D.L., Hansen, L.N., Mackwell, S., Tasaka, M., Heidelbach, F., Leinenweber, K., 2018. Transport properties of olivine grain boundaries from electrical conductivity experiments. Contrib. Mineral. Petrol. 173 (5), 41. https://doi.org/10.1007/s00410-018-1468-z.
Praus, O., Pěčová, J., Petr, V., Babuška, V., Plomerová, J., 1990. Magnetotelluric and seismological determination of the lithosphere-asthenosphere transition in Central Europe. Phys. Earth Planet. Inter. 60 (1), 212–228. https://doi.org/10.1016/0031-9201(90)90262-V.
Rodi, W., Mackie, R.L., 2001. Nonlinear conjugate gradients algorithm for 2-D magnetotelluric inversion. Geophysics 66 (1), 174–187. https://doi.org/10.1190/1.1444893.
Santos, F.A.M., Mateus, A., Almeida, E.P., Pous, J., Mendes-Victor, L.A., 2002. Are some of the deep crustal conductive features found in SW Iberia caused by graphite? Earth Planet. Sci. Lett. 201 (2), 353–367. https://doi.org/10.1016/S0012-821X(02)00721-5.
Schmucker, U., 1973. Regional induction studies: a review of methods and results. Phys. Earth Planet. Inter. 7 (3), 365–378. https://doi.org/10.1016/0031-9201(73)90061-7.

Seifert, K.F., Will, G., Voigt, R., 1982. Electrical conductivity measurements on synthetic pyroxenes $MgSiO_3$–$FeSiO_3$ at high pressures and temperatures under defined thermodynamic conditions. In: Schreyer, W. (Ed.), High-pressure Researches in Geoscience. Schweizerbartsche, Stuttgart, pp. 419–432.

Selway, K., 2014. On the causes of electrical conductivity anomalies in tectonically stable lithosphere. Surv. Geophys. 35 (1), 219–257. https://doi.org/10.1007/s10712-013-9235-1.

Selway, K., Sheppard, S., Thorne, A.M., Johnson, S.P., Groenewald, P.B., 2009. Identifying the lithospheric structure of a Precambrian orogen using magnetotellurics: the Capricorn Orogen, Western Australia. Precambrian Res. 168 (3–4), 185–196. https://doi.org/10.1016/j.precamres.2008.09.010.

Selway, K., O'Donnell, J.P., Özaydin, S., 2019. Upper mantle melt distribution from petrologically constrained magnetotellurics. Geochem. Geophys. Geosyst. 20 (7), 3328–3346. https://doi.org/10.1029/2019GC008227.

Selway, K., Smirnov, M.Y., Beka, T., O'Donnell, J.P., Minakov, A., Senger, K., Falede, J.I., Kalscheuer, T., 2020. Magnetotelluric constraints on the temperature, composition, partial melt content and viscosity of the upper mantle beneath Svalbard. Geochem. Geophys. Geosyst. https://doi.org/10.1029/2020GC008985 e2020GC008985.

Sifré, D., Gardés, E., Massuyeau, M., Hashim, L., Hier-Majumder, S., Gaillard, F., 2014. Electrical conductivity during incipient melting in the oceanic low-velocity zone. Nature 509 (7498), 81–85. https://doi.org/10.1038/nature13245.

Stegena, L., Géczy, B., Horváth, F., 1975. Late Cenozoic evolution of the Pannonian basin. Tectonophysics 26 (1-2), 71–90. https://doi.org/10.1016/0040-1951(75)90114-6.

Strangway, D.W., Swift Jr., C.M., Holmer, R.C., 1973. The application of audio-frequency magnetotellurics (AMT) to mineral exploration. Geophysics 38 (6), 1159–1175. https://doi.org/10.1190/1.1440402.

Szabó, Cs, Bodnar, R.J., 1996. Changing magma ascent rates in the Nógrád-Gömör volcanic field Northern Hungary/Southern Slovakia: evidence from CO_2-rich fluid inclusions in metasomatized upper mantle xenoliths. Petrology 4 (3), 221–230.

Szabó, Cs, Bodnar, R.J., 1998. Fluid-inclusion evidence for an upper-mantle origin for green clinopyroxenes in late Cenozoic basanites from the Nógrád-Gömör Volcanic Field, northern Hungary/southern Slovakia. Int. Geol. Rev. 40 (9), 765–773. https://doi.org/10.1080/00206819809465237.

Szabó, Cs, Bodnar, R.J., Sobolev, A.V., 1996. Metasomatism associated with subduction-related, volatile-rich silicate melt in the upper mantle beneath the Nograd-Gomor volcanic field, northern Hungary/southern Slovakia; evidence from silicate melt inclusions. Eur. J. Mineral. 8 (5), 881–899.

Szabó, Cs., Taylor, L.A., 1994. Mantle petrology and geochemistry beneath the Nógrád-Gömör Volcanic Field, Carpathian-Pannonian Region. Int. Geol. Rev. 36, 328–358. https://doi.org/10.1080/00206819409465465.

Tari, G., Báldi, T., Báldi-Beke, M., 1993. Paleogene retroarc flexural basin beneath the Neogene Pannonian Basin: a geodynamic model. Tectonophysics 226 (1-4), 433–455. https://doi.org/10.1016/0040-1951(93)90131-3.

Tašárová, A., Afonso, J.C., Bielik, M., Götze, H.J., Hók, J., 2009. The lithospheric structure of the Western Carpathian–Pannonian Basin region based on the CELEBRATION 2000 seismic experiment and gravity modelling. Tectonophysics 475 (3–4), 454–469. https://doi.org/10.1016/j.tecto.2009.06.003.

Tian, Z.Z., Liu, J., Xia, Q.K., Ingrin, J., Hao, Y.T., Christophe, D., 2017. Water concentration profiles in natural mantle orthopyroxenes: a geochronometer for long annealing of xenoliths within magma. Geology 45 (1), 87–90. https://doi.org/10.1130/G38620.1.

Tikhonov, A.N., 1950. On determining electrical characteristics of the deep layers of the Earth's crust. In: Dokl. Akad. Nauk., vol. 73 SSSR, pp. 295–297.

Tomek, Č., 1993. Deep crustal structure beneath the central and inner West Carpathians. Tectonophysics 226 (1–4), 417–431. https://doi.org/10.1016/0040-1951(93)90130-C.

Tommasi, A., Tikoff, B., Vauchez, A., 1999. Upper mantle tectonics: three-dimensional deformation, olivine crystallographic fabrics and seismic properties. Earth Planet. Sci. Lett. 168 (1-2), 173–186. https://doi.org/10.1016/S0012-821X(99)00046-1.

Varentsov, I.M., Sokolova, E.Y., Martanus, E.R., Nalivaiko, K.V., the BEAR working group, 2003. System of electromagnetic field transfer operators for the BEAR array of simultaneous soundings: methods and results. Izvestiya Phys. Solid Earth 39 (2), 118–148.

Vozár, J., Jones, A.G., Fullea, J., Agius, M.R., Lebedev, S., Le Pape, F., Wei, W., 2014. Integrated geophysical-petrological modeling of lithosphere-asthenosphere boundary in central Tibet using electromagnetic and seismic data. Geochem. Geophys. Geosyst. 15 (10), 3965–3988. https://doi.org/10.1002/2014GC005365.

Wang, D., Mookherjee, M., Xu, Y., Karato, S.I., 2006. The effect of water on the electrical conductivity of olivine. Nature 443 (7114), 977. https://doi.org/10.1038/nature05256.

Wannamaker, P.E., Jiracek, G.R., Stodt, J.A., Caldwell, T.G., Gonzalez, V.M., McKnight, J.D., Porter, A.D., 2002. Fluid generation and pathways beneath an active compressional orogen, the New Zealand Southern Alps, inferred from magnetotelluric data. J. Geophys. Res. Solid Earth 107 (B6). https://doi.org/10.1029/2001JB000186. ETG-6.

Weaver, J.T., Agarwal, A.K., Lilley, F.E.M., 2000. Characterization of the magnetotelluric tensor in terms of its invariants. Geophys. J. Int. 141 (2), 321–336. https://doi.org/10.1046/j.1365-246x.2000.00089.x.

Wiese, H., 1962. Geomagnetische Tiefentellurik Teil II: Die Streichrichtung der untergrundstrukturen des elektrischen Widerstandes, erschlossen aus geomagnetischen Variationen. Geofisica pura e applicata 52 (1), 83–103. https://doi.org/10.1007/BF01996002.

Wilshire, H.G., Shervais, J.W., 1975. Al–augite and Cr–diopside ultramafic xenoliths in basaltic rocks from western United States. In: Physics and Chemistry of the Earth. Pergamon, pp. 257–272. https://doi.org/10.1016/B978-0-08-018017-5.50024-9.

Xia, Q.-K., Liu, J., Kovács, I., Hao, Y.T., Li, P., Yang, X.Z., Chen, H., Sheng, Y.M., 2019. Water in the upper mantle and deep crust of eastern China: concentration, distribution and implications. Natl. Sci. Rev. 6 (1), 125–144. https://doi.org/10.1093/nsr/nwx016.

Xu, Y., Shankland, T.J., Duba, A.G., 2000. Pressure effect on electrical conductivity of mantle olivine. Phys. Earth Planet. Inter. 118 (1–2), 149–161. https://doi.org/10.1016/S0031-9201(99)00135-1.

Yang, X., Keppler, H., McCammon, C., Ni, H., Xia, Q.-K., Fan, Q., 2011. Effect of water on the electrical conductivity of lower crustal clinopyroxene. J. Geophys. Res. Solid Earth. https://doi.org/10.1029/2010JB008010.

Yoshino, T., Matsuzaki, T., Shatskiy, A., Katsura, T., 2009. The effect of water on the electrical conductivity of olivine aggregates and its implications for the electrical structure of the upper mantle. Earth Planet. Sci. Lett. 288 (1–2), 291–300. https://doi.org/10.1016/j.epsl.2009.09.032.

Yoshino, T., Shimojuku, A., Shan, S., Guo, X., Yamazaki, D., Ito, E., Higo, J., Funakoshi, K.I., 2012. Effect of temperature, pressure and iron content on the electrical conductivity of olivine and its high-pressure polymorphs. J. Geophys. Res. Solid Earth 117 (B8). https://doi.org/10.1029/2011JB008774.

Zajacz, Z., Kovacs, I., Cs, Szabo, Halter, W., Pettke, T., 2007. Evolution of mafic alkaline melts crystallized in the uppermost lithospheric mantle: a melt inclusion study of olivine-clinopyroxenite xenoliths, northern Hungary. J. Petrol. 48 (5), 853–883. https://doi.org/10.1093/petrology/egm004.